

Mesoscale Mechanics of Reactive Materials for Enhanced Target Effects

Performance/Technical Report 2011

Report I-56/11

Prepared by:

N. Durr
G. Heilig
A. Klomfass
M. Sauer

Management:

A. Klomfass

February 2012
Freiburg, Germany

Mesoscale Mechanics of Reactive Materials for Enhanced Target Effects

Performance/Technical Report 2011

Report I-56/11

Ordering Customer	Office of Naval Research
Project Number	277 118
Award Number	N00014-11-1-0307
Classification	Restricted Distribution

Prepared by:

Dr. G. Heilig
Research Fellow – Computational Physics

N. Durr
Research Fellow – Computational Physics

Management:

Dr. A. Klomfass
Principal Investigator

Dr. M. Sauer
Group Manager – Computational Physics

Prof. Dr. S. Hiermaier
Head of Department – Dynamics in Microstructures

Prof. Dr. K. Thoma
Director of Ernst-Mach-Institut

Table of Contents

1	Introduction	4
1.1	Short Summary of Achievements from the Previous Grant	5
1.2	Progress in the Ongoing Grant – Overview	6
2	Boundary Conditions for Fragment Acceleration	9
2.1	Objectives and Approach	9
2.2	Numerical Models in 2-D	9
2.2.1	Results from 2-D Simulations	11
2.3	Summary of 2-D Simulation Results	21
2.4	Results of 3-D Simulations	24
3	Mesoscale Launch and Impact Simulations	27
3.1	Objectives and Computational Methods	27
3.2	Generation of Representative Volume Elements	28
3.3	Analyses of Scaling Effects in Tension Simulation	29
3.4	Analyses of Scaling Effects in Fragmentation Simulation	31
3.5	Material Modeling	33
3.6	Initial Selection of Material Data Sets	34
3.7	Launch Modeling	36
3.8	Launch Simulations of a Single Cube	38
3.9	Impact Modeling	43
3.10	Launch and Impact Simulations and Fragment Analysis	44
4	Conclusions and Next Steps	50
5	Literature	52

1 Introduction

It is known that the combustion of metal powder within detonation products or shock-heated air significantly increases the overall energy of a blast weapon [1], [5]. Important factors for this effect are the grain size and ignition temperature of the combustible material. In order to investigate the mechanical behavior of reactive materials (RM) on the mesoscale, EMI has been awarded two grants from the Office of Naval Research: a first grant awarded in June 2007 for a performance period until December 2009, and the current grant awarded in March 2011 for a performance period until June 2012. The central objective of the research is to develop and apply methodologies for the analysis and prediction of fragmentation of reactive materials. These methodologies can be used as a basis to tailor material fabrication processes for specific applications, e. g. by selecting parameters like initial grain size distribution, porosity, sintering pressure and temperature.

Specifically, the projects were motivated by the aim to design (metallic) materials, which fragment under certain dynamic loading conditions into small particles, which can chemically react with a suitable ambient medium, such as shock-heated ambient air or hot detonation products. Such materials could be effectively used to devise new or improved weapons with enhanced mechanical and/or thermal effects, Figure 1.1.

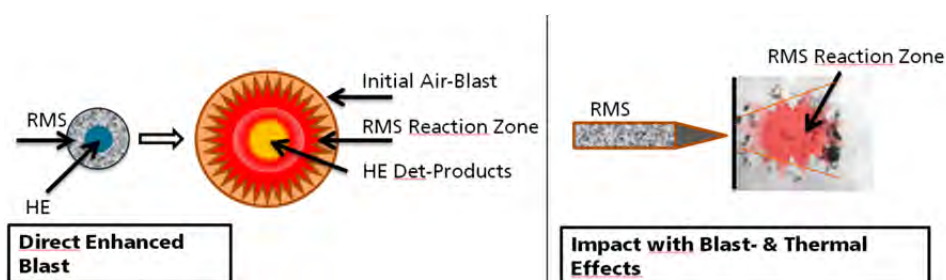


Fig. 1.1: Two principle applications of reactive material structures (RMS) in which a fine fragmentation is crucial for enhanced weapon effects.

A first status report has been delivered to ONR as part of a written overview for the 2011 peer review of the *ONR 351 Advanced Energetic Materials and Advanced Combustion Program*. This is the second status report. A final report will be delivered after the end of the current grant in July 2012.

1.1 Short Summary of Achievements from the Previous Grant

In the first grant, the aim envisaged was the development and validation of numerical methods for the mechanical simulation of materials at grain scale. These methods shall enable the predictive analysis of the dependencies of the mechanical properties – especially the fragmentation behavior – on the morphological and constitutive nature of a material at grain scale. Simulation capability of this kind can be effectively applied to design new materials with optimized mechanical properties.

The desired simulation capability comprised two aspects. First, a computational method had to be available that allowed the parameter-controlled generation of **representative volume elements (RVEs)** of the considered materials with realistic microstructures. This included the task of generating computational meshes of these microstructures. Secondly, a finite-element solver for continuum mechanical conservation equations was needed, which permitted a three-dimensional, time-dependent simulation of the response of a RVE to external loads, including a treatment of inter-granular failure and fragmentation. Within this project, suitable methods for both aspects have been further developed towards the required capabilities.

An experimental investigation of suitable model materials was performed for the validation of the developed methods and models. The selection and procurement of model materials and the conduction of microstructural analysis, various characterization tests – especially fragmentation tests – were also part of this project.

The results achieved can be summarized as follows: As the goal of the project was the development of computational and experimental tools and models with a focus on mesostructural mechanical aspects, copper (Cu) and iron (Fe) powders were selected as inert reference materials. From these materials, a variety of cold-pressed and subsequently sintered samples with different porosities were produced. Mixtures of CuFe (50:50 volume ratio) were also manufactured. An extensive testing program was realized for the manufactured materials. It comprised, among others, static and dynamic tensile tests, impact tests such as inverse Taylor tests and planar plate tests, and cube impact tests on aluminum plates. The experimental results served as a basis for the mesomechanical modeling, in particular for the identification of mesoscale material parameters and for model validation.

In order to obtain realistic mesostructural models, RVEs were generated based on statistical evaluation of micrographs taken from the material samples. The commercial software GEODICT from Fraunhofer ITWM has been used for that purpose. In addition, the new software GEOSTAT has been developed by EMI, which is less versatile than GEODICT but particularly capable of constructing parameter-controlled RVEs for the currently investigated microstructures.

Static tensile tests served as a base for the development of a mesoscale material model (grain scale) of the sintered structures. The mechanical properties of the metallic grains and of the artificially inserted grain boundaries around them were chosen such that simulated tensile curves reproduced the experimental measurements. As a validation step, a homogenized (continuum) material model was derived from mesomechanical simulations and used to simulate compression tests.

Fragmentation of three material variants was analyzed in mesomechanical cube impact simulations. A good qualitative accordance with experimental observations was reached. As simulation tools the commercial software LS-DYNA had been used and a new finite-element code especially developed for mesostructural analysis has been extended.

1.2 Progress in the Ongoing Grant – Overview

The current research, which is documented in detail in the following chapters of this report, builds directly on the methodologies that were developed in the first grant. It is closer to navy applications, i. e. the improvement of the effectiveness of anti-aircraft or anti-missile warheads by using reactive materials.

Although a number of candidate materials have been proposed and tested for this purpose, e. g. mixtures of PTFE and aluminum, [5], the development of a material which combines the desired properties

- sufficient strength to withstand explosive launch
- sufficient weight for effective perforation
- fine grained fragmentation upon impact
- reactivity of fragments
- low production costs

is still an open issue. As mentioned above, sintered metallic powders are potential candidates and offer a number of adjustable properties which depend on the raw materials they consist of (e. g. aluminum, magnesium and tungsten), their initial state (e. g. grain size distribution) and fabrication parameters (e. g. pressures and temperatures applied during sintering).

A promising choice for the reactive material constituents are aluminum and tungsten, as tungsten offers high ballistic effectiveness while aluminum offers high reactivity. The aim of the current research is the identification of suitable microstructures of tungsten-Al mixtures by means of computational mesoscale analyses. These microstructures shall survive an explosive launch in a conventional warhead, effectively perforate a thin target and fragment into very small particles upon perforation of the target.

For this purpose, the explosive launch of metal cubes in the warhead has to be simulated on the mesoscale. In order to obtain the relevant loading conditions (fluid pressures), the pressure loads are determined in macroscale simulations of the launch process. The simulation software ANSYS AUTODYN with fluid-structure interaction is used for this task. The obtained pressure transients are then applied in mesoscale RVE simulations to determine deformation and possibly damage and material failure acquired in the launch process.

The metal cube used here as a representative example for a pre-fabricated fragment has an edge length of 1 cm and is composed of grains of about 30 μm radius. As the grains need to be adequately resolved in the computation, an edge length of finite elements of 3 μm is adequate. Therefore, about 37 billion elements would be needed to discretize an entire cube. This goes beyond the numerical capabilities available today. To overcome this limitation, scaling laws are used to bridge meso- and macroscale.

Figure 1.2 gives an overview on the tasks of the current grant. As the scaling might alter simulated fragment size distributions, it is checked under which conditions the scaling holds and how the computed results might need to be scaled up to be representative for full-size samples. A first result is that scaled impact computations appear to give representative fragmentation statistics if the RVE edge length is at least four times larger than the obtained average fragment size. Thus, the chosen scaling will be checked carefully at each future computation in order to improve it if necessary.

Once the scaling has been established, systematic parameter variation is used to find materials that survive launch and fragment upon perforation of the target (task 2). For this purpose mesoscale simulations of launch and impact are performed in which the mesoscale structure (material composition, grain size distribution, porosity, mechanical behavior of grain interfaces) is varied. A variety of the mesoscale launches and impact simulations with pure tungsten and aluminum RVEs – including the analysis of fragmentation – has been performed so far. It turns out, that aluminum RVEs do not survive the accelerations during the explosive launch; they fail (fragment to a large degree) almost immediately after ignition of the high explosive. The tungsten RVEs, however, in general survive the launch and can thus be further investigated with respect to their perforation/fragmentation performance in the impact phase.

The next steps will include the analysis of the launch behavior of mixtures of the both materials. This task is currently ongoing. The best performing materials will be checked for their behavior under different impact conditions (parameters will be impact angle, impact velocity, plate thickness and plate material).

The task 3, the generalization of the obtained material design, will be performed after task 2 is finished, in the first half of the year 2012. The results will be documented in the final report in July 2012.

The results achieved so far and the next steps are given in more detail at the end of this report.

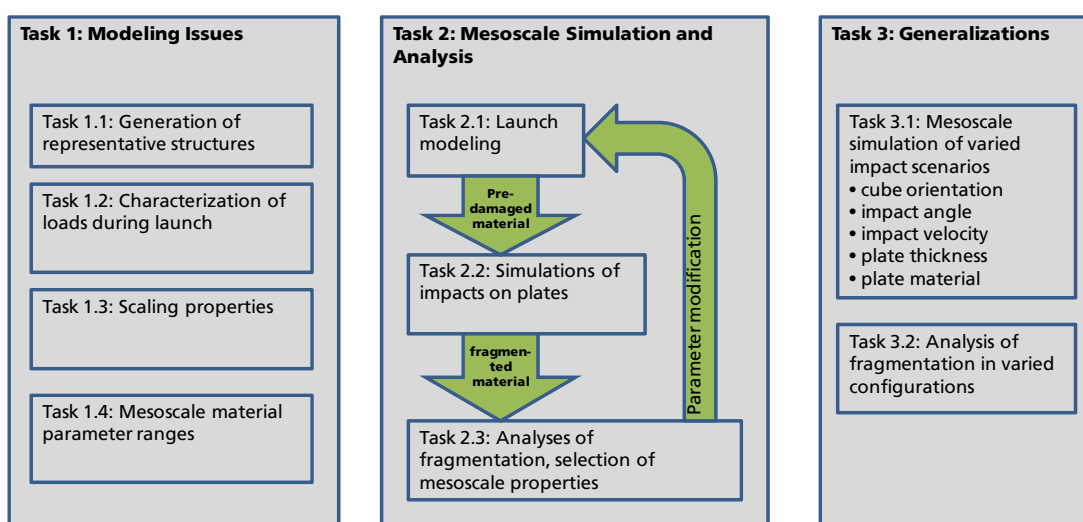


Fig. 1.2: Overview on tasks.

2 Boundary Conditions for Fragment Acceleration

2.1 Objectives and Approach

In order to determine realistic loading conditions for pre-formed fragments during explosive launch from a warhead casing, a generic warhead configuration is analyzed on the macroscale. The pressure-time histories obtained from the macroscale simulations can be directly used as boundary conditions in the subsequent mesoscale simulations for the analysis of the material response to this loading.

For the simulations described in this chapter, the commercial software ANSYS-AUTODYN has been used. In order to evaluate the pressures acting on the pre-formed fragments during the explosive launch, we use a simplified model where material failure and erosion are excluded. In the macroscale model, the cubes are treated as homogenous bodies composed of a single material with properties of pure tungsten or pure aluminum or mixtures of these. The considered mixtures are 50 volume percent tungsten and 50 volume percent aluminum (Al/Tun 50/50) and 83 volume percent aluminum and 17 volume percent tungsten (Al/Tun 83/17). The majority of the simulations use a two-dimensional model of a warhead cross section; the validity of this simplification is checked by comparison with results from a selected three-dimensional simulation.

2.2 Numerical Models in 2-D

Figure 2.1 shows the numerical setup of the fully coupled Euler-Lagrange simulations in two dimensions. In total, 32 Lagrangian parts (dark blue) – consisting of aluminum or tungsten or mixtures of these – are placed at a radius of 52.5 mm around a TNT cylinder (light blue). The detonation initiation point is exactly in the axis of the TNT cylinder and has the coordinates (0, 0). The TNT and the air (green) are modeled in the Eulerian part, which ranges from -250 mm to 250 mm in x- and y-direction and consists of quadratic elements of 0.5 mm edge length. All Lagrangian parts, which represent the metal cubes, are also quadratic with a size of 10 mm and contain 10 elements in each direction (edge length = 1.0 mm); each Lagrangian part therefore consists of 100 finite elements in total. Thus, the resolution of the Eulerian part is twice as fine as that of the Lagrangian parts. The TNT is modeled using the JWL-equation of state with density $\rho = 1.63 \text{ g/ccm}$ and detonation velocity 6930 m/s. The air is treated as an ideal gas of constant specific heats (adiabatic coefficient $\gamma = 1.40$).

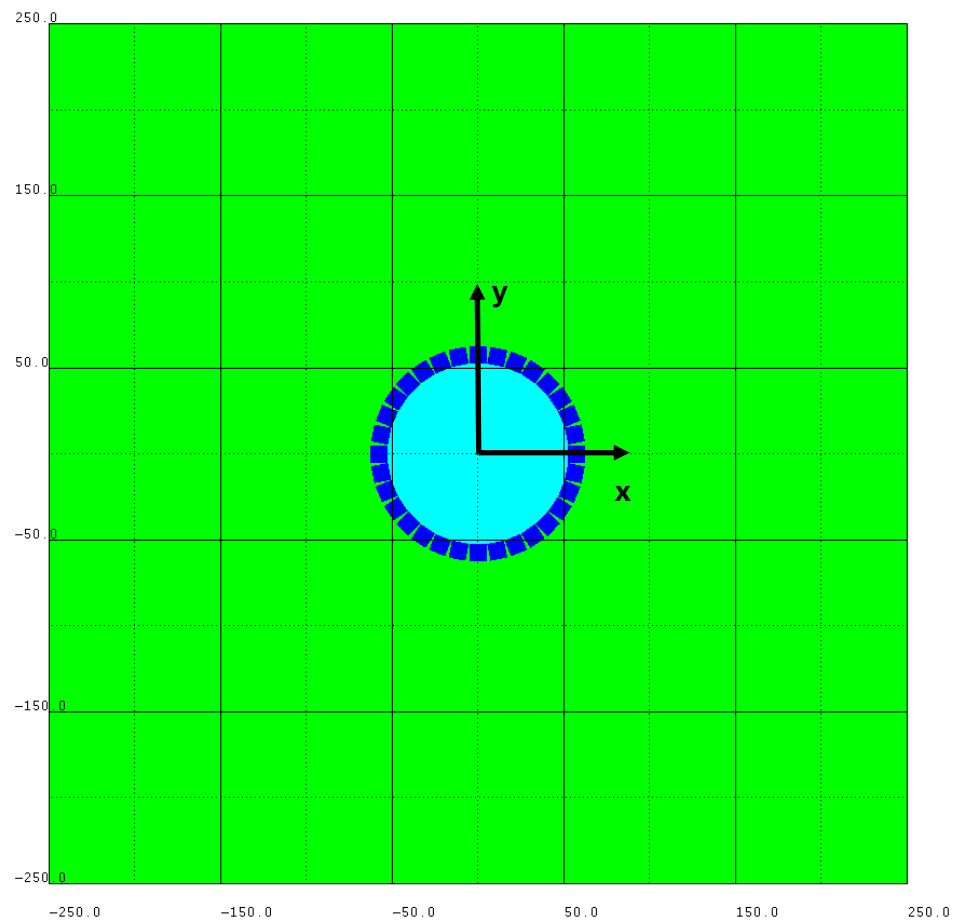


Fig. 2.1: Numerical setup for the 2-D fluid-structure coupled simulation of the fragment acceleration.

The aluminum (Al 7039) and the tungsten (Tun) cubes as well as the cubes made of the mixtures Al/Tun 50/50 and Al/Tun 83/17 are treated as elastic-plastic bodies with strain hardening. Failure and erosion are not considered here as the material response is analyzed in detail in the subsequent mesoscale simulations. The Steinberg-Guinan model is applied which gives expressions for the shear modulus and the yield strength as functions of effective plastic strain, pressure and internal energy for the investigated materials [7]. As equation of state a Mie-Gruneisen model is used. All material parameters used here are listed in Table 2.1.

Table 2.1: Material parameters for the four metals. Al/Tun 50/50 and Al/Tun 83/17 are volumetric mixtures of Al7039 and tungsten. The tungsten material with porosity (10 % or 20 %) has the same data as the tungsten material without porosity.

	Al 7039	Tun	Al/Tun 50/50	Al/Tun 83/17	Tun 10 % porosity	Tun 20 % porosity
Density [g/ccm]	2.77	19.30	11.035	5.5175	19.30	19.30
Gruneisen coeff. Γ_0 [1]	2.00	1.67	1.835	1.9439	1.67	1.67
C_1 [m/s]	5328.0	4030.0	4679	5107.34	4030	4030
S_1 [1]	1.338	1.237	1.2875	1.3208	1.237	1.237
Yield stress Y_0 [kPa]	3.37 e5	2.2 e6	1.2685e6	6.5371e5	2.2 e6	2.2 e6
Shear modulus G_0 [kPa]	2.76 e7	1.6 e8	9.38 e7	5.011 e7	1.6 e8	1.6 e8

The parameters for the two mixture materials Al/Tun 50/50 and Al/Tun 83/17 are generated through volumetric averaging of the respective aluminum and tungsten parameters. The following formula for the mean density $\bar{\rho}$ of the mixture yields

$$\bar{\rho} = y_{Al} \rho_{Al} + y_{Tu} \rho_{Tu} = \frac{V_{Al}}{V_{tot}} \rho_{Al} + \frac{V_{Tu}}{V_{tot}} \rho_{Tu} \quad ; \quad y_{Al} + y_{Tu} := 1$$

where V_{tot} denotes the total volume of the fragment; y denotes volume fractions.

All material properties are estimated by volume weighted averages, see Table 2.1. For the present purposes, this establishes a sufficiently accurate material model.

2.2.1 Results from 2-D Simulations

Figure 2.2 shows the computed isopycnics (lines of constant density) in the Eulerian part at two different times after ignition of the TNT. The propagation of the

gaseous detonation products through the metallic cubes and the radially outward movement of the cubes can be clearly recognized. In front of the detonation products, a shock wave in the atmospheric air builds up. The pressures and densities between the fragments are the highest in the flow field. Although the setup is symmetric at time zero, the resulting air shock and the contact lines are not. This is a consequence of the fluid-dynamic instabilities and the finite approximation on the Cartesian grid.

Figure 2.3 shows the velocities during the launch phase for the different materials. After approximately 100 μs , the acceleration of the fragments tends to zero and the final velocity is reached. Due to the different masses (densities) of the fragments, the final velocities differ significantly. The final velocity of an aluminum cube is 2012 m/s and therefore 2.34 times higher than that of a tungsten cube. The final velocities of the cubes made of the two Al/Tun mixtures fall consistently between the velocities of the aluminum and the tungsten cubes.

Figure 2.4 presents the time histories of the pressures p (black curves) and the three stresses σ_{xx} , σ_{yy} , σ_{xy} (colored curves, see Figure 2.1 for axis-orientation) in the aluminum and in the tungsten cube, evaluated in the “middle-bottom” element (see Fig. 2.5 below). The values in the tungsten cube are approximately 1.5 times higher than in the aluminum cube. This can be explained by the larger mass of the tungsten cubes; thus the ring of these cubes expands slower, which in consequence leads to higher pressures in the detonation gases, which act on the cubes surfaces.

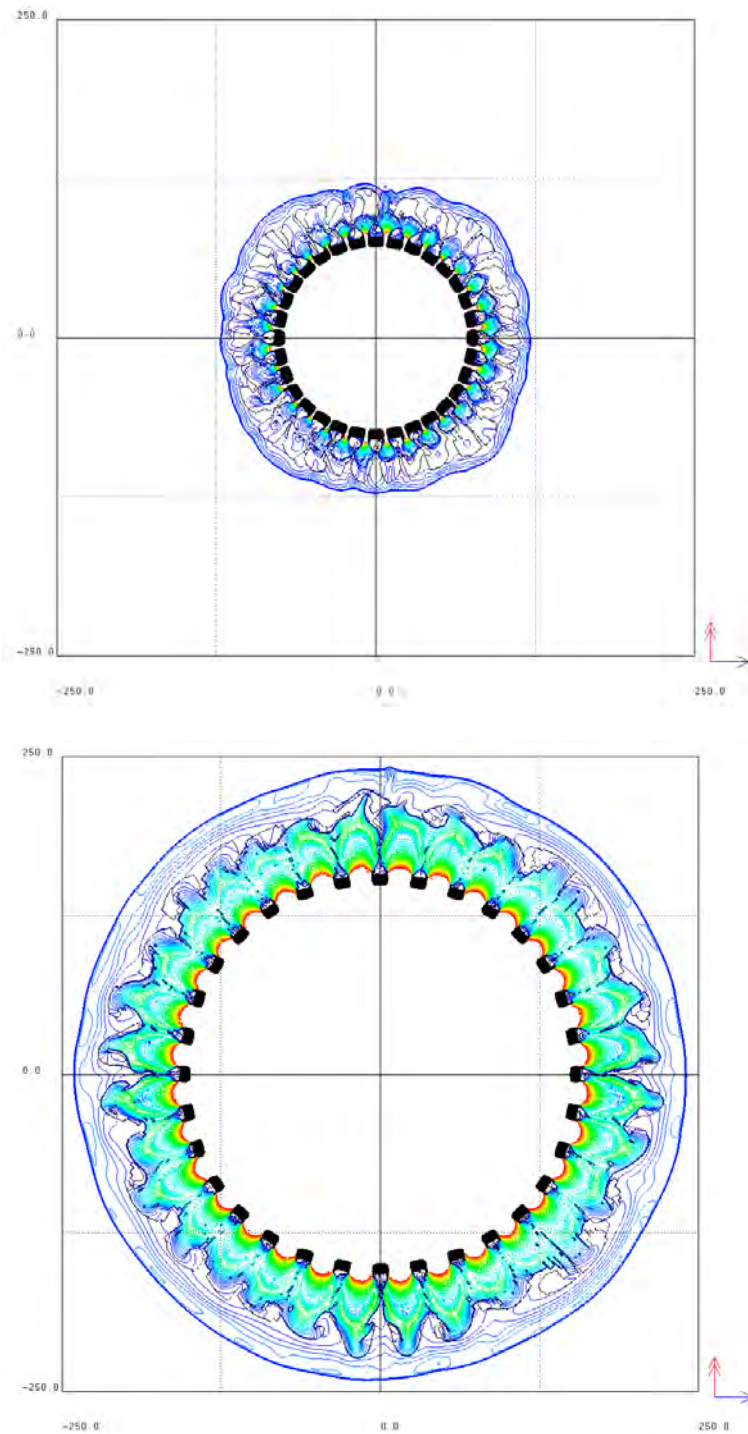


Fig. 2.2: Density field at $t = 20 \mu\text{s}$ (above) and $t = 60 \mu\text{s}$ (below) after ignition of the TNT cylinder.

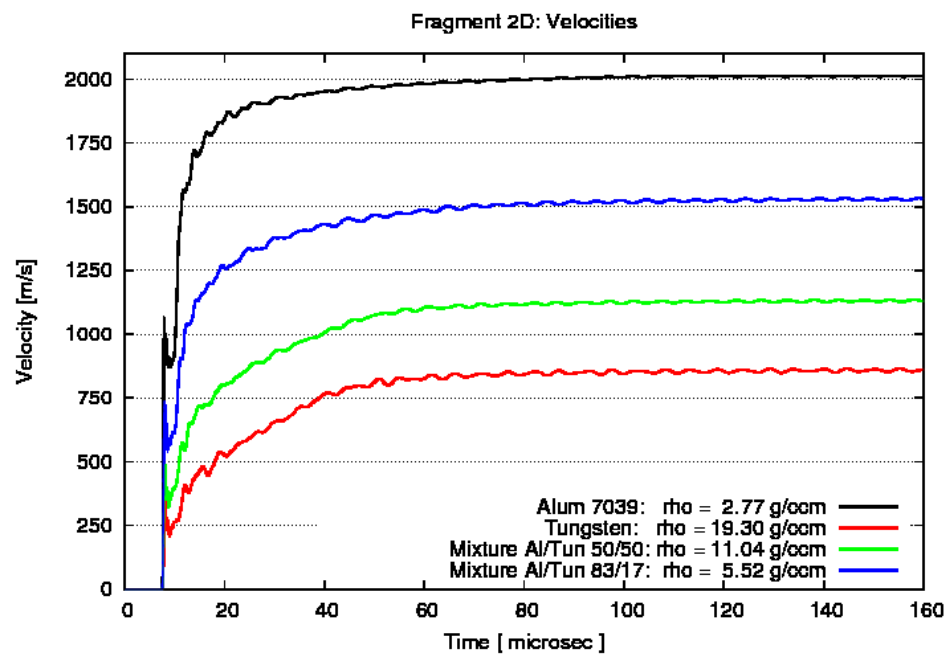


Fig. 2.3: Absolute velocities of the four metallic cubes: Al 7039, tungsten, Al/Tun 50/50, Al/Tun 83/17. The end of the acceleration or launch phase can be defined at $t = 125 \mu\text{s}$.

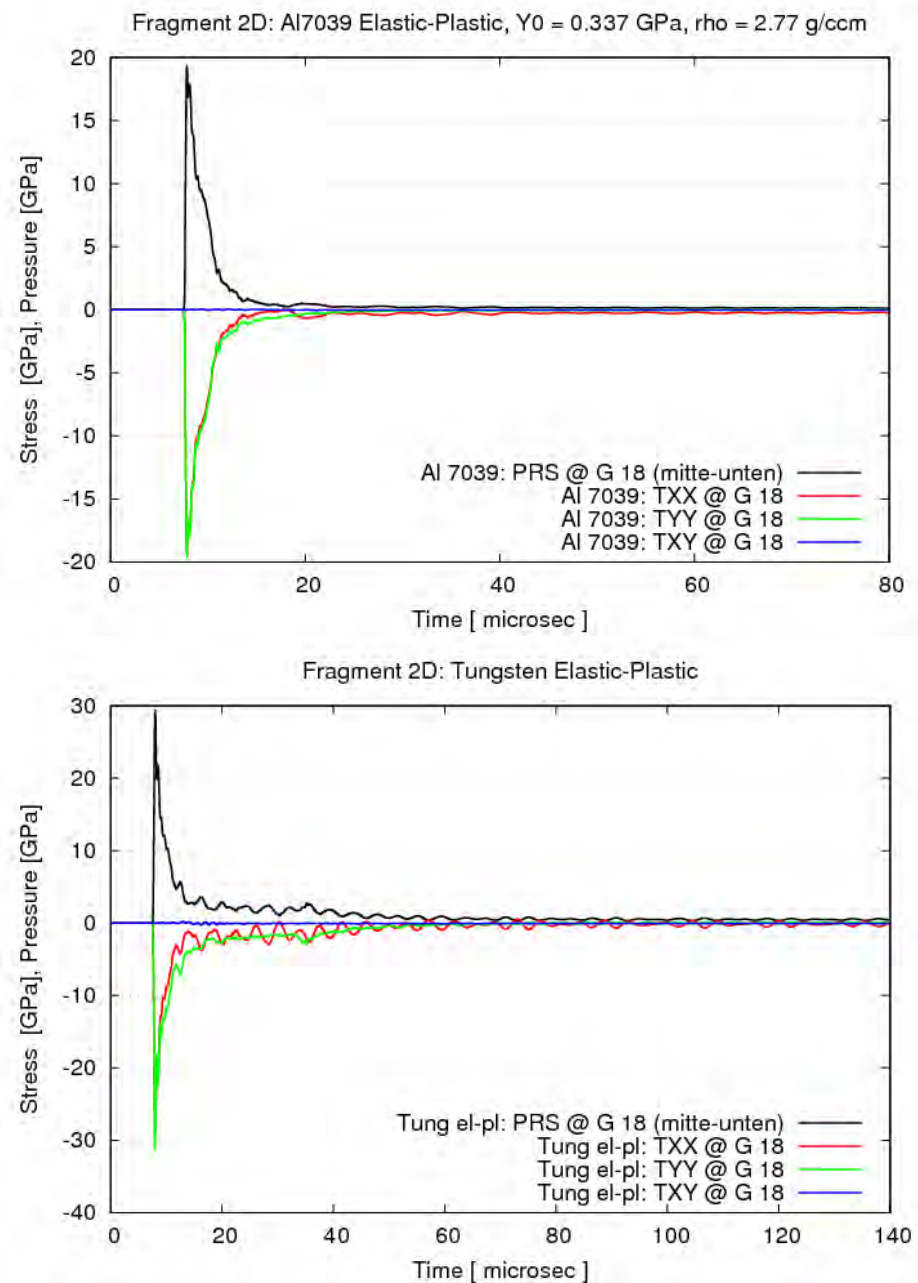


Fig. 2.4: Stress and pressure histories in the aluminum and tungsten cubes.

The two pictures of Figure 2.5 show the pressure fields of three cubes (above: Al7039; below: tungsten) and their immediate surroundings in the Eulerian mesh 40 μs after ignition of the TNT. Note that the shapes of the aluminum and the tungsten fragments differ according to the different material properties. Furthermore, the distance between the aluminum fragments is greater than the distance between the tungsten fragments as a consequence of the different masses (inertia). It is obvious that the pressures in the outer cells of each fragment are not equal to the gas pressures in the Eulerian mesh due to material strength. Therefore, the recorded histories shown in Figure 2.4 cannot be used directly as boundary conditions representing the fluid dynamics loads during launch.

Instead of this, the gas pressure in the Eulerian mesh has been evaluated at six characteristic points. Four points are the centers of each cube face. These six points are denoted TOP, BOTTOM, LEFT MIDDLE, LEFT BELOW, RIGHT MIDDLE and RIGHT BELOW in Figure 2.5. They represent numerical gauges moving with the considered cube through the Eulerian mesh. During the first 60 μs of the process, a sampling rate of 1.0 μs was used; for later times the sampling rate has been decreased. The results are shown in the Figures 2.6 and 2.7.

Figure 2.6 presents the gas pressures acting on the TOP and the BOTTOM faces of the cube (left) and the difference pressures (right), i. e. pressure on the BOTTOM border minus pressure on the TOP border. It turns out that the TOP pressure is by a factor of approx. 100 smaller than the BOTTOM pressure and therefore does not significantly influence the acceleration of the fragments. The diagrams also confirm that the launch phase duration is about 100 μs in accordance with the velocity trends seen in Figure 2.3.

Figure 2.7 gives the gas pressures acting on the LEFT MIDDLE and the RIGHT MIDDLE borders of the aluminum (left diagram) and the tungsten (right diagram) cubes. The pressure curves almost coincide as it should be; a lateral acceleration (x-direction) of the fragments does not take place.

Figure 2.8 refers to the positions LEFT BELOW and RIGHT BELOW of the cubes. Again, the two pressure curves almost coincide but are about the factor 4 higher than the pressure data shown in Figure 2.7. Nevertheless, the pressures acting on the BOTTOM of the fragments are significantly higher than all other pressures and are therefore the most relevant for the launch process under consideration.

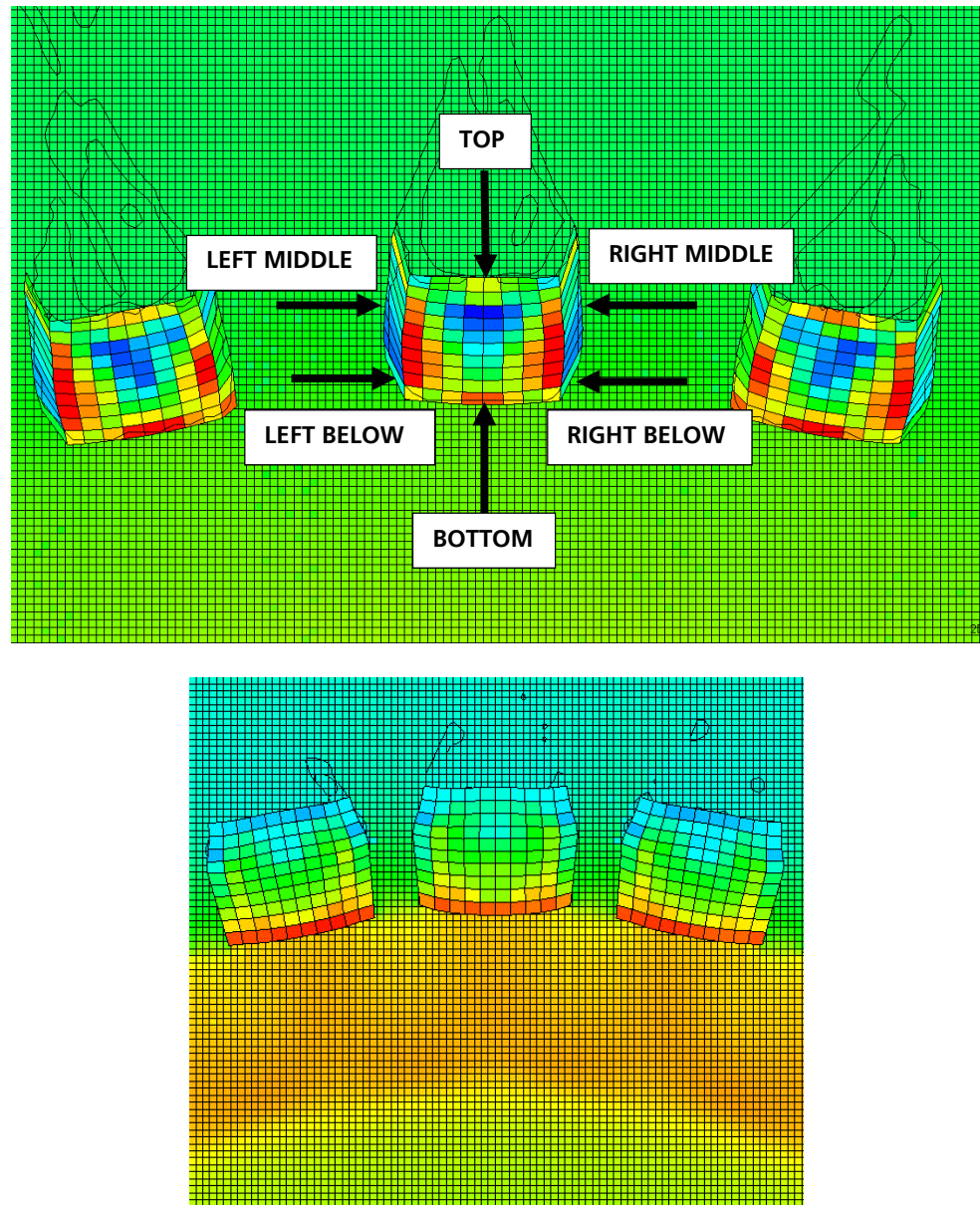


Fig. 2.5: Enlarged view onto aluminum cubes (above) and tungsten cubes (below) in the Eulerian mesh 40 μ s after ignition. The colors represent the static pressure; red: high pressure, blue: low pressure. Positions of points where the fluid pressure is evaluated.

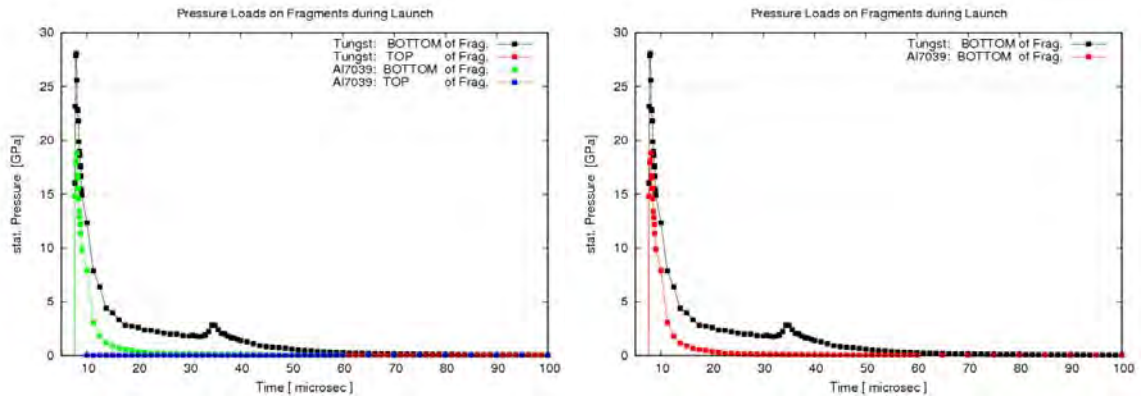


Fig. 2.6: Pressure histories at the TOP and the BOTTOM point of the cube in the Eulerian mesh.

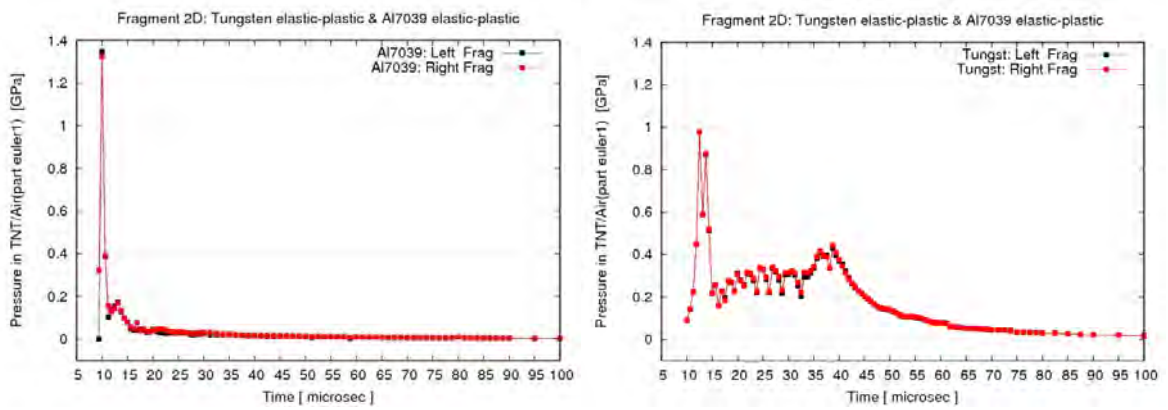


Fig. 2.7: Pressure histories (left: Al7039, right: tungsten) at the LEFT MIDDLE and the RIGHT MIDDLE point of the cube in the Eulerian mesh.

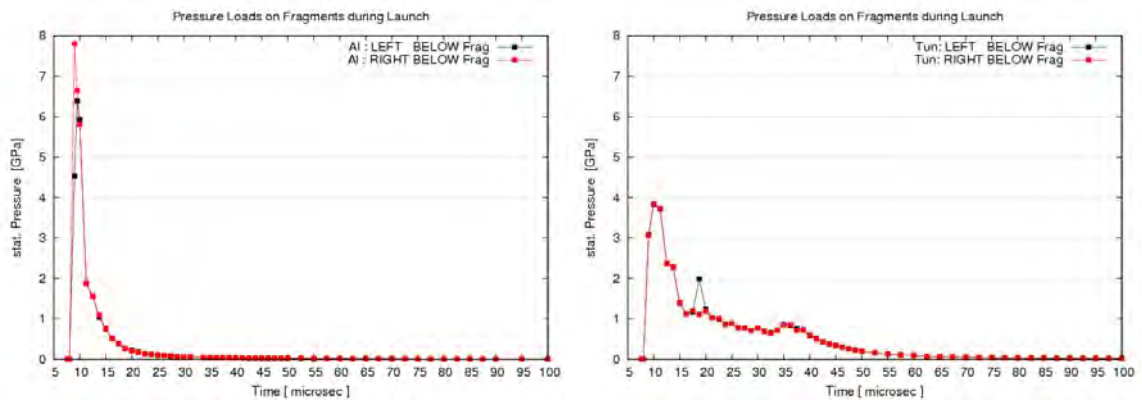


Fig. 2.8: Pressure histories (left: Al7039, right: tungsten) at the LEFT BELOW and the RIGHT BELOW point of the cube in the Eulerian mesh.

The pressure curves of both figures are taken as basis for the time-dependent boundary conditions to be used in the mesoscale simulation of the launch phase.

In order to check the pressure data evaluated on the BOTTOM and the TOP of a cube, the average radial velocity of a cube (here evaluated in y-direction) $v_{y,ave}$ is taken from the computation and is differentiated with respect to time t . Multiplying this average radial acceleration with the factor m/A (mass of the cube divided by the bottom area) yields the average pressure $p_{y,ave}$ acting on the part in the radial direction:

$$p_{y,ave} = \frac{m}{A} \frac{d}{dt} v_{y,ave} \quad .$$

The Figure 2.9 shows the comparison between the average pressures obtained with the formula above (red curves) and the evaluated pressure difference of the BOTTOM and TOP pressures acting on the border of the part (green curves). It can be seen that for tungsten (right diagram) and for aluminum (left diagram), the two curves coincide well. This result is a good verification for the chosen method to determine the correct boundary conditions for the accelerated cubes in the launch phase.

Further to the above materials (solid tungsten, aluminum and mixtures of these), we have investigated the launch process of cubes made of porous tungsten with porosities of 10 % and 20 %. This has been done in order to investigate the effects of smaller variations of density. As we expect the fragment density to be the dominant material parameter for the loading conditions, we simply eroded some elements from a solid cube such that the desired average densities were obtained. The results for the calculated velocity-time histories are shown in Figure 2.10.

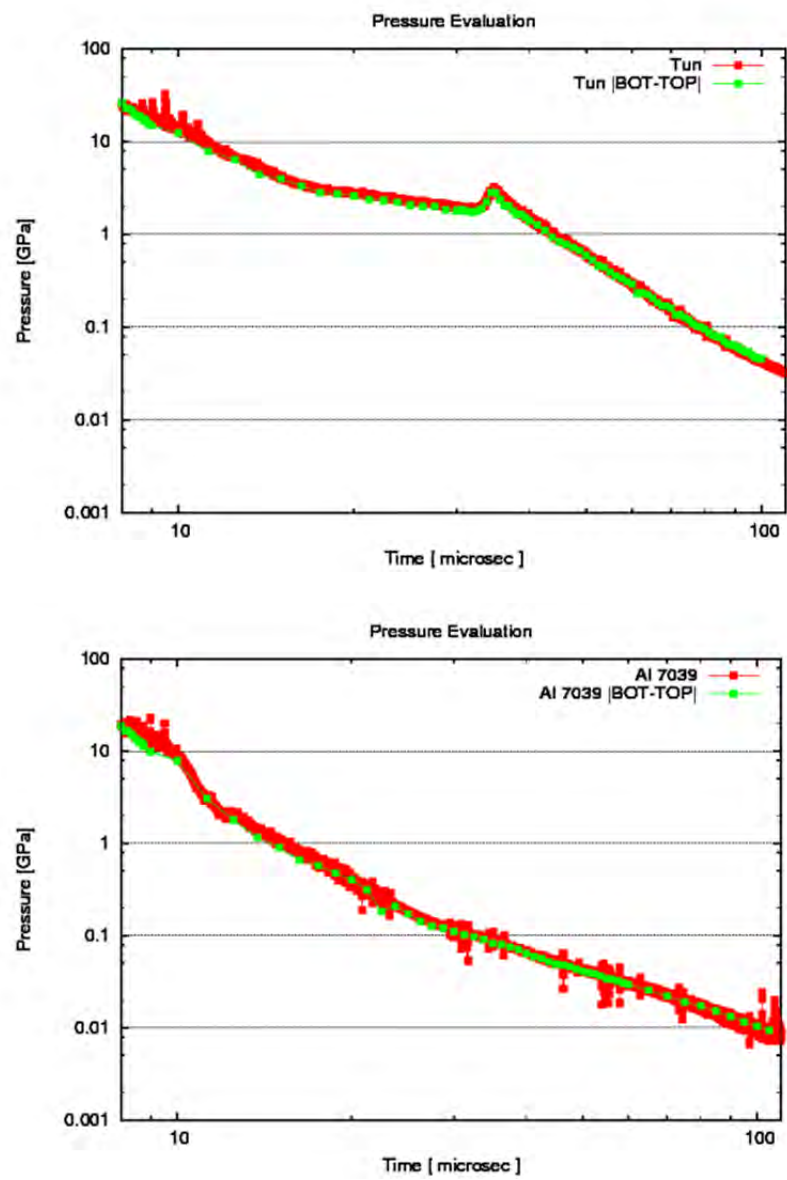


Fig. 2.9: Averaged pressures (red) and evaluated difference pressures (green) for tungsten (left diagram) and for aluminum (right diagram).

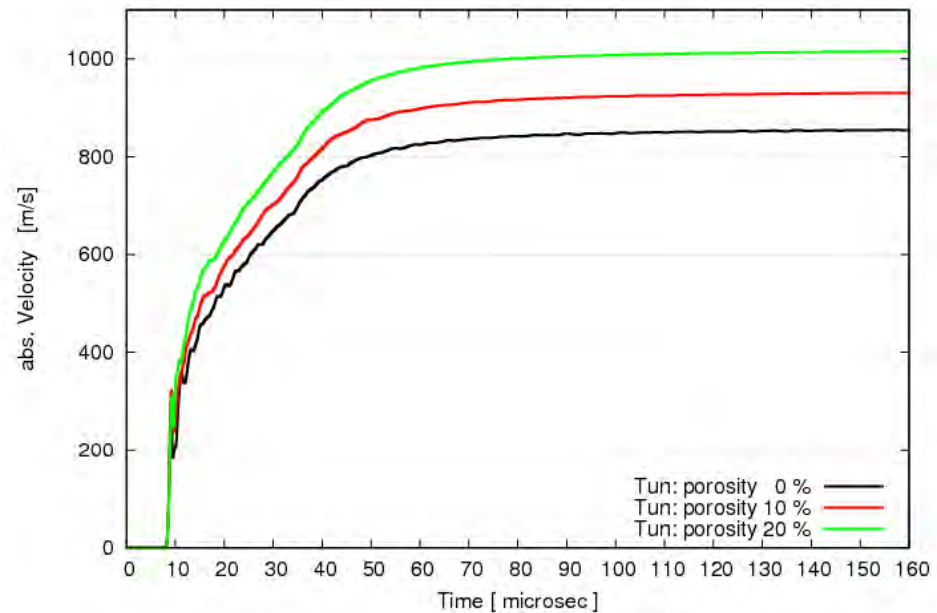


Fig. 2.10: Velocities of tungsten cubes with the porosities 0 %, 10 % and 20 %.

2.3 Summary of 2-D Simulation Results

The results obtained with the two-dimensional fluid-structure-coupled approach are summarized in Figure 2.11, which shows the relevant pressure transients acting on the investigated cubes. The data are presented in non-logarithmic (above) and in logarithmic scale (below).

It is evident that the presented difference pressures (pressure on the BOTTOM of the cube minus pressure on the TOP of the cube) are highest for the homogeneous tungsten ($\rho = 19.30 \text{ g/ccm}$, black curve) and lowest for the homogeneous aluminum ($\rho = 2.77 \text{ g/ccm}$, red curve). The curves for two volumetric mixtures Alu/Tun 50/50 ($\rho = 11.035 \text{ g/ccm}$, green curve) and Alu/Tun 83/17 ($\rho = 5.5175 \text{ g/ccm}$, blue curve) lay between the black and the red curve.

Furthermore, the influence of the porosity is comparably small as it was expected. The respective curves (magenta and cyan) almost coincide with the black curve (0 % porosity) in the chosen presentation.

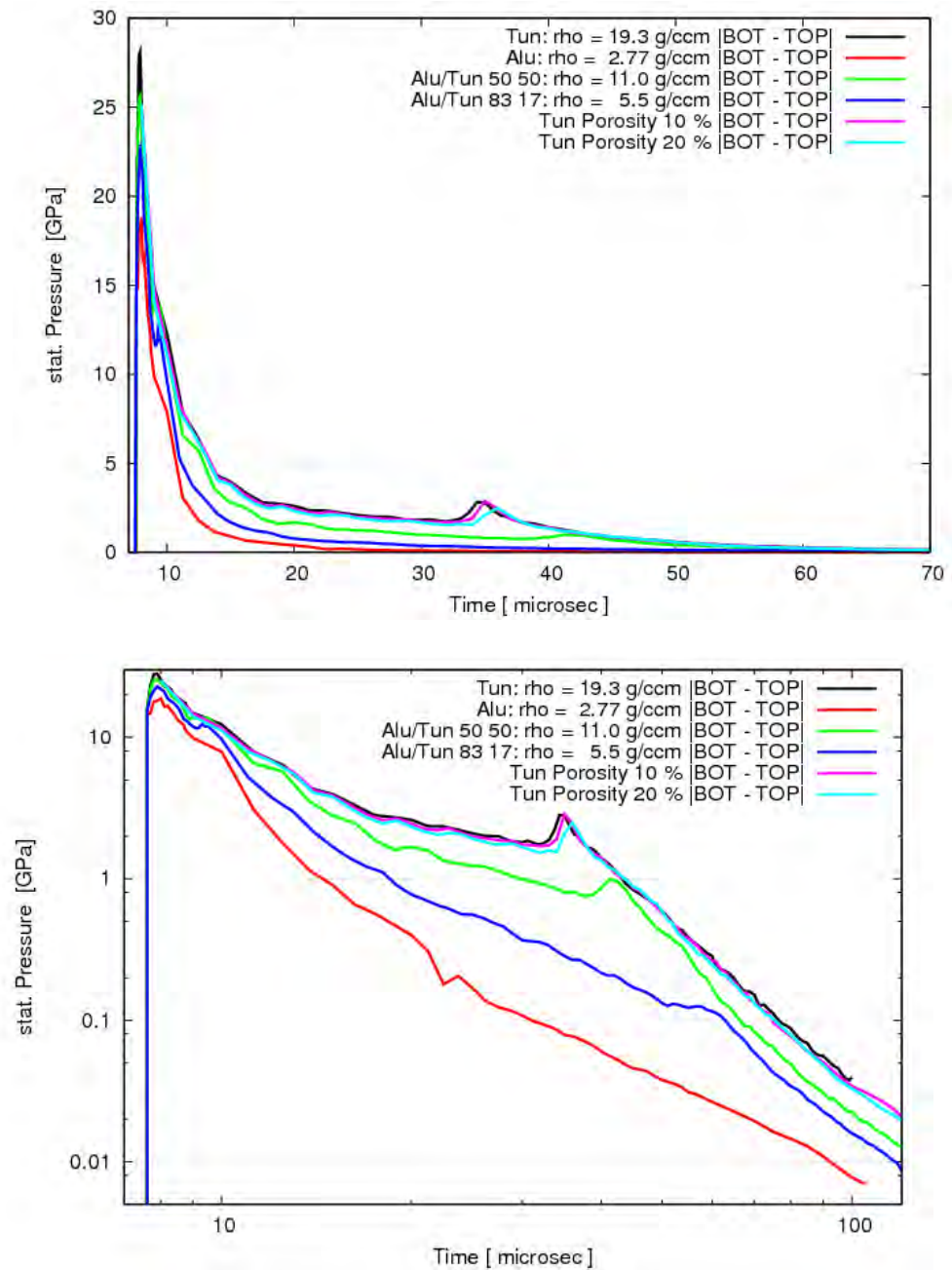


Fig. 2.11: Difference pressures (BOTTOM of the cube minus TOP of the cube) acting on the six cubes in non-logarithmic (above) and in logarithmic scale (below).

Figure 2.12 summarizes the effect of density of the cubes on the total momentum transfer for the investigated configuration with 1 cm cubes places onto a TNT charge with 52 mm radius.

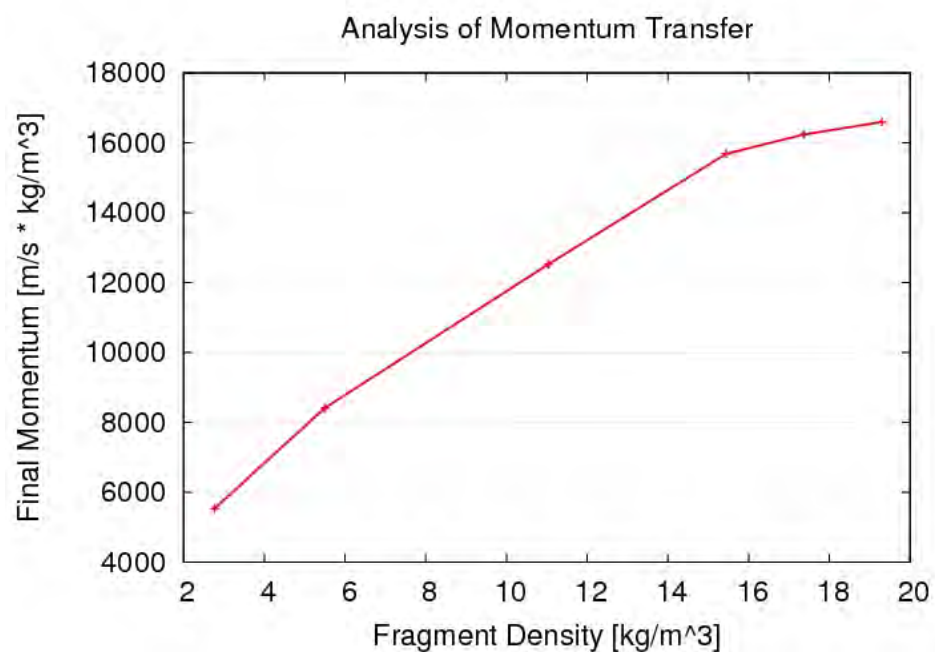


Fig. 2.12: Total momentum transfer to the pre-fabricated fragments (cubes with 1 cm edge lengths) places onto cylindrical TNT charge with radius 52 mm.

An important observation for the mesoscale simulations of the launch process is depicted in Figure 2.13. It shows that due to elastic-plastic deformation, the individual cubes stay in contact during the initial phase of the launch process. Thereby, they partly seal the gas volume during this time interval and also limit their further lateral deformation through their mutual lateral support.

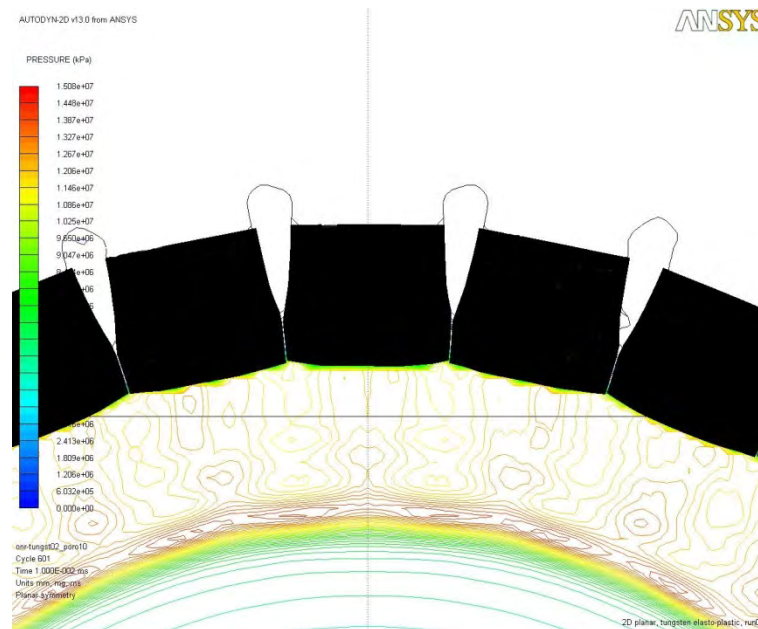


Fig. 2.13: Contact of adjacent cubes throughout extended time interval due to deformation (example for tungsten cubes).

2.4 Results of 3-D Simulations

In order to check the applicability of the two-dimensional approach, a 3-D model has been developed. In general, the physics of the process investigated can be described more accurately in three dimensions, but the resolution of the meshes cannot be chosen as fine as in 2-D due to the high computational effort in 3-D. Especially the Eulerian part has to be realized with coarser resolution.

Figure 2.14 left shows the corresponding numerical model in three dimensions. It consists of one Eulerian part (dark blue represents air) and in total 306 Lagrangian parts (red) for the metallic cubes, which are again concentrically placed in a radius of 52.5 mm around the TNT cylinder (green) inside. In order to make the fragments visible, only half of the Eulerian part is shown. The Eulerian part has the dimensions 300 mm, 150 mm, 300 mm in xyz-direction and is built up with $200 \times 100 \times 200 = 2$ million elements. The cubes have 10 mm edge length and a spatial resolution of 2 mm (125 elements). At $y = 0$, a symmetry plane is placed to reduce the computational effort.

The right picture of Figure 2.14 shows the computed pressure field at the edges of the Eulerian part and the accelerated cubes (light blue) 40 μ s after the lateral

ignition of the TNT cylinder. The detonation point (black circle in Figure 2.14, left) is not placed in the middle of the cylinder but in the middle of one of its lids. Due to the non-symmetric ignition in the 3-D model, each of the 17 circular layers of fragments is accelerated differently.

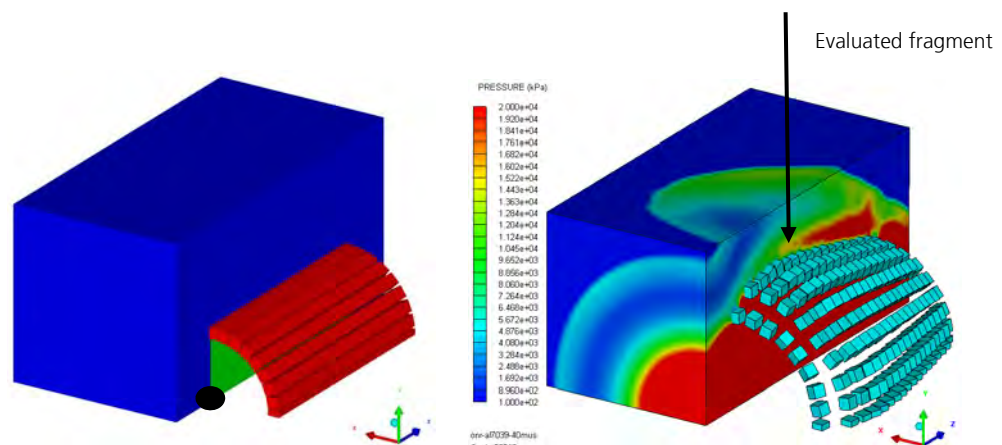


Fig. 2.14: Left: Numerical model for the 3-D simulations. The $y = 0$ plane is the symmetry plane of the model, the right half of the Euler mesh (dark blue) is not visible in order to show the arrangement of the fragments (red) and the TNT cylinder (green). The black circle left of the TNT cylinder indicates the detonation point. Right: Computed pressures in the Euler part and positions of the fragments 40 μ s after ignition.

The velocities of the cubes are evaluated and compared to the corresponding velocities of the 2-D model, see Figure 2.15. Here, the absolute velocity of the 3-D model is taken from a cube in the middle layer, see right picture of Figure 2.14. In the 2-D computations, the final velocities of the aluminum and the tungsten cubes (red curves) are slightly (about 10 %) higher than the final velocities in the 3-D computations (black curves). This is due to the different geometry of the detonation wave in three dimensions and the possibility of the cubes to separate in the axial direction. Note that the movement of the fragments in the 3-D computation starts later than that of the 2-D computation. This results from the greater distance between the evaluated cube and the detonation point.

As the difference between 2-D and 3-D is small compared to the differences arising from the choice of the material and the fluid pressures acting on the cubes surfaces can be evaluated much more precisely from the 2-D computations due to the higher resolution, the 2-D results will be used exclusively in the following.

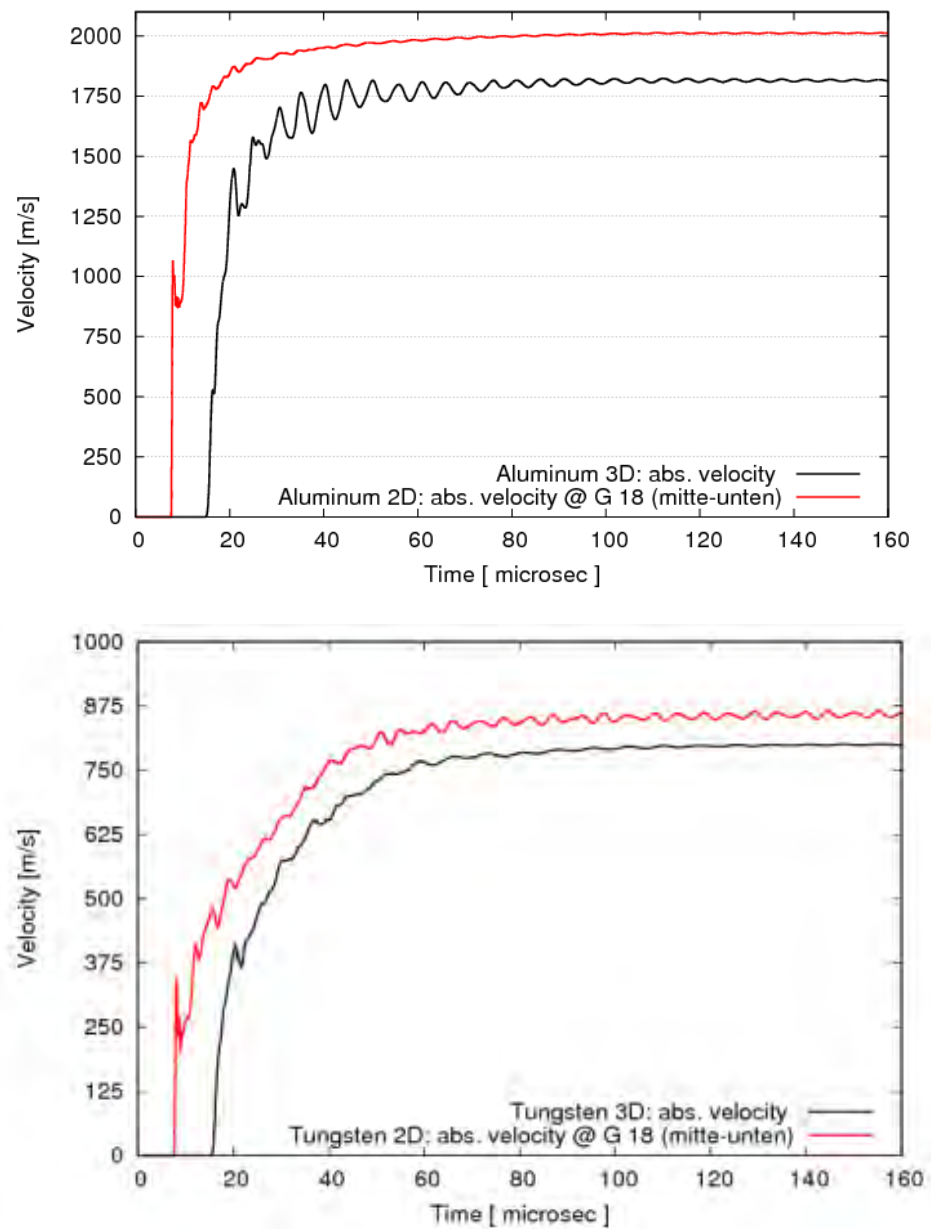


Fig. 2.15: Comparison of the absolute velocities of the cubes in the 2-D simulation (red curves) and the 3-D simulation (black curves).

3 Mesoscale Launch and Impact Simulations

3.1 Objectives and Computational Methods

The performed mesoscale simulations aim to assess the material behavior of the investigated candidate materials under launch and impact conditions. Particularly, it shall be clarified which materials withstand the severe acceleration during the explosive launch and how those materials fragment upon perforation of the selected thin target.

The computational method used for the mesoscale simulations is based on hexahedral finite-element models of the pre-formed fragments (cubes) which resolve the material microstructure. Inter-granular failure is computationally treated with a node-split algorithm. The required methods are implemented in the commercial code LS-DYNA, which was used for all simulations in this project. It is one of the two approaches that have been developed in the previous grant [6]. The second approach, which is based on tetrahedral elements in combination with interface elements, is realized in the research software MESOFEM. This is, however, not yet applicable to impact processes as a contact algorithm has not been implemented so far.

The size of the bodies that can be considered in mesoscale simulations is restricted by the required computational effort. Therefore, the launch and impact simulations are performed with down-sized cubes. Instead of using the true size 1 cm cubes as in the macroscopic simulations, sub-millimeter sized cubes will be considered here. The geometrical scaling rules which are being applied are summarized in the following table.

In our approach, the geometric dimensions are scaled, velocities and material parameters expressed in terms of stresses and pressures remain unchanged. If a strain rate parameter appears in the material model, the respective parameter would need to be adopted since the strain rate scales with $1/\lambda$ (λ being the geometric scaling ratio). However, applicability of this procedure is restricted to linear strain rate dependence.

The geometrical scaling is applied only for the outer dimensions of the cube and the target plate. The granular structure (e. g. grain size distribution) itself is NOT scaled. The result is a smaller structure with fewer grains, which can be computationally analyzed. However, it is an open question whether the fragment size distributions computed with this type of scaling are still representative for the original size. Therefore, the scaling effects were further investigated (Section 3.4).

Table 3.1: Geometrical scaling with scaling factor λ and resulting scaling rules for selected derived quantities.

Basic quantities	Symbol	Dimension	Scaling
Length	L	L	$\lambda \cdot L$
Mass	M	M	$\lambda^3 \cdot M$
Time	T	t	$\lambda \cdot L$
Temperature	T	T	T
Derived quantities			
Velocity	v	L / t	v
Acceleration	a	L / t^2	a / λ
Density	ρ	M / V^3	ρ
Force	F	$M \cdot L / t^2$	$\lambda^2 \cdot F$
Energy	E	$M \cdot L^2 / t^2$	$\lambda^3 \cdot E$
Pressure, stress	p, σ	$M / (L \cdot t^2)$	p, σ
Strain	ε	L / L	ε
Strain rate	$\dot{\varepsilon}$	$L / (L \cdot t)$	$\dot{\varepsilon} / \lambda$

3.2 Generation of Representative Volume Elements

The mesoscale RVEs shall represent granular metallic structures produced by cold-pressing and sintering. They are generated with the software GEOSTAT developed at EMI within the previous grant. It serves to create voxel-based cubes with a distribution of spheres that represent the grains. The implemented algorithm places a defined number of spheres with defined size distribution in a cubic volume such that overlapping occurs.

To achieve a desired volume fraction, spheres with the highest radius are placed first followed by spheres with incrementally decreasing radius, because smaller spheres are more likely to fill the remaining voids. As soon as all spheres are placed in the cube, GEOSTAT maps the spheres into a user-defined Cartesian grid. If two or more spheres are present in a cell, the sphere with the highest cell volume fraction will be attributed to the cell. As last step, a growth/shrinking process of the spheres is performed, such that the user-defined porosity can be calibrated.

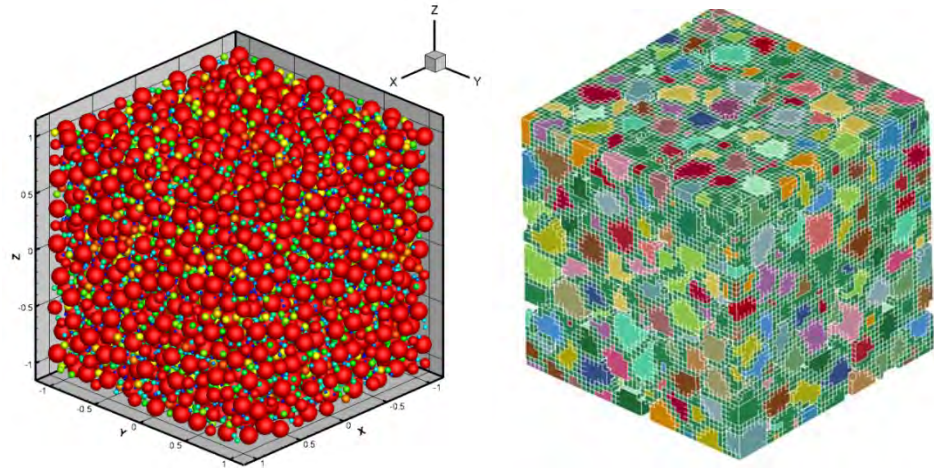


Fig. 3.1: Left: Distribution of spheres according to the placement method. Right: Cartesian mesh of a RVE, the colors indicate individual grains.

In order to obtain RVEs with different structures, two parameters have been varied:

- Grain size distribution: two cases are considered, one with constant grain size, one with varying grain size.
- Porosity: RVEs with 10 % and 20 % porosity were generated.

Once the structure has been generated with GEOSTAT, grain boundaries are inserted according to the methodology developed in the previous grant [14]. Thereby, pseudo-material is inserted between the grains, the yield stress of which is lower than that of the grains. This is done by replacing elements adjacent to the neighboring grains. A further step in the modeling establishes an inter-granular failure criterion. This consists of defining a critical strain on the adjacent elements of the inter-granular nodes, above which all of these elements separate from each other (node-split technique). This failure model enables the formation of inter-granular cracks.

3.3 Analyses of Scaling Effects in Tension Simulation

In order to ensure the representativeness of the RVE, the RVE size has to be chosen such that it contains a sufficiently high number of grains. The effects of scaling on fragmentation results will be assessed in the next Section 3.4. This section deals with a more basic requirement, i. e. the representativeness of the RVE for quasi-static tensile loading.

From experiences in the previous grant, the minimum RVE edge length shall be larger than about 10 grains per edge. Additionally, in view of the establishment of scaling laws, several RVE sizes are investigated. Departing from a big structure, smaller structures are extracted from the bigger one by keeping the same resolution (identical element size), see Figure 3.2.

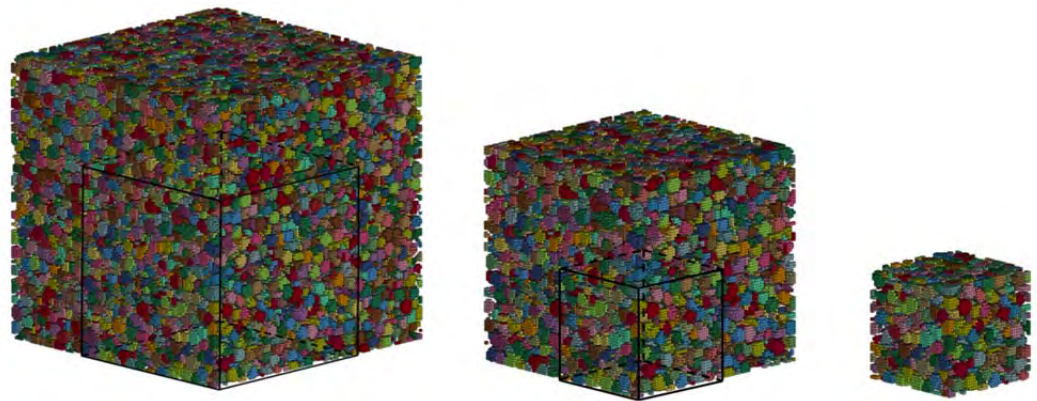


Fig. 3.2: Three RVE sizes with extraction process. From left to right: $L = 0.9$ mm, $L = 0.6$ mm, $L = 0.3$ mm. For better visibility, the border material has been blanked.

The RVEs with edge length of $L = 0.9$ mm, $L = 0.6$ mm and $L = 0.3$ mm were generated, where the smaller RVEs are sub-volumes extracted from the largest RVE as shown in Figure 3.2. The mesh resolution (finite-element size) is $L_{\text{element}} = 7.5 \mu\text{m}$, which corresponds to 120, 80 and 40 elements per edge, respectively. If the smallest structure fulfills the representativeness requirements, so do the bigger ones as they contain more grains. An average grain diameter of $D = 30 \mu\text{m}$ was assumed, therefore, the criterion of minimum number of 10 grains per edge is satisfied for all three RVEs. For the model with “uniform” grain size distribution, the diameter of the spheres used in the grain generation process is exactly $D = 30 \mu\text{m}$ for all spheres. The resulting grain size distribution is, however, not strictly uniform. For the “non-uniform” grain distribution, the diameter of the generating spheres is defined in the interval $D = [7.5 \mu\text{m}, 45 \mu\text{m}]$. This interval is consistent with the representativeness conditions as the smallest grain diameter equals or is higher than the element resolution. The chosen interval is centered on $D_{\text{middle}} = 26.25 \mu\text{m}$. The slightly smaller average size allows a better insertion of the smaller spheres in-between the bigger ones.

To check the representativeness of the smaller cubes extracted from the big one, quasi-static uniaxial tensile tests were performed with each cube. Tungsten was selected as material used in these tests, material data will be given in Section 3.5. The boundary conditions were adjusted such that an identical strain development

over time was realized. Figure 3.3 shows the stress-strain responses of the tensile test for each edge length. One can observe very similar stress-strain responses until the peak stress (failure point) is reached. The post-failure behavior is not of interest here and is expected to differ due to the differing reference (cube) lengths. This result proves, at least in the quasi-static tensile regime, that the smaller cubes represent the behavior of the big cube well.

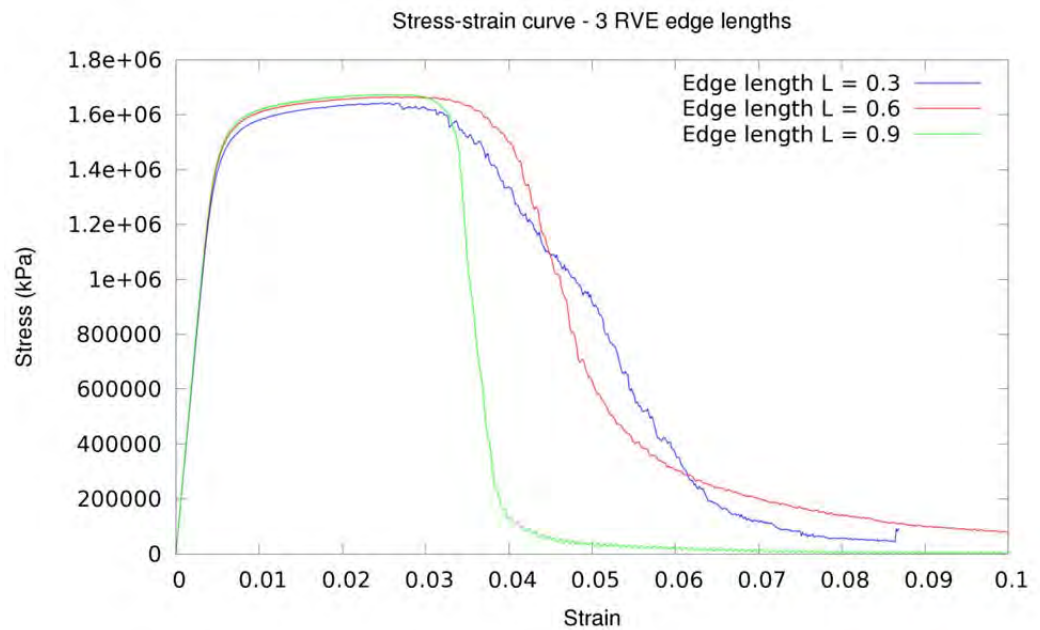


Fig. 3.3: Stress-strain response for three RVE edge lengths 0.9 mm, 0.6 mm, 0.3 mm.

3.4 Analyses of Scaling Effects in Fragmentation Simulation

The effects of scaling were further investigated for the impact process. This phase is considered more critical with respect to scaling than the launch phase as the fragmentation characteristics upon impact should be much more sensitive to scaling than the failure thresholds relevant for the launch phase.

The fragmentation of cubes with two edge lengths, 0.4 mm and 0.2 mm, upon impact on plates of thickness 0.1 mm and 0.05 mm, respectively, is simulated for three different velocities, an additional case with 0.8 mm cube edge length and 0.2 mm plate thickness is simulated for one velocity. The investigated materials are taken from [6]. It is important to mention again that the scaling was done on the cube and plate dimensions only whereas the grain sizes and their distribution

remained the same. In fact, the 0.2 mm cube has been obtained as a sub-volume of the 0.4 mm cube.

The analysis of the fragmentation is based on the average fragment volume obtained from the impact simulations. This average fragment volume was defined as the median of the cumulative fragment volume distribution.

Table 3.2: Average fragment volume (in $0.001 \cdot \text{mm}^3$) after impact of RVE against aluminum plate. Top: CuFe 300 MPa; bottom: Fe 580 MPa. Cases for which the average fragment volume is approximately unaffected by the scaling are marked green, other cases yellow.

CuFe 300 MPa Unit: $0.001 \cdot \text{mm}^3$	v = 634 m/s	v = 1600 m/s	v = 2600 m/s
L = 0.4 mm	0.169	0.109	0.093
L = 0.2 mm	0.257	0.106	0.094
Fe 580 MPa Unit: $0.001 \cdot \text{m}^3$	v = 475 m/s	v = 1600 m/s	v = 2600 m/s
L = 0.8 mm	–	283.2	–
L = 0.4 mm	54.5	30.1	0.118
L = 0.2 mm	7.18	3.69	0.117

For both materials, at the velocity of 2600 m/s, an identical average fragment volume for both cube dimensions was obtained. The same can be said for 1600 m/s for the mixture sample. For all other cases, deviations between both scales occur and no direct relation between fragment size and scale can be explicitly formulated. From this it can be concluded that there is an upper limit of the average fragment volume (or a lower limit of the impact velocity) beyond which the scaling significantly affects the fragmentation results. The cubic root of the average fragment volume can be taken as a measure for the effective fragment size. Using this measure, the ratio of the effective fragment size to the cube length can be set up as a simple criterion for the validity of the scaling. In our case, the scaling seems to hold for values of this ratio up to 0.25, which means that the scaling is only valid if the cube edge length is at least four times larger than the obtained effective fragment size, see Table 3.3. Although this criterion can only be evaluated after the fragmentation calculation, it can serve to verify the computed results. Further simulations with 0.8 mm cubes will be performed to further analyze the applicability of the criterion.

Table 3.3: Effective fragment size/cube length ratio (rounded values) after impact of RVE against aluminum plate. Top: CuFe 300 MPa; bottom: Fe 580 MPa. Cases for which the average fragment volume is approximately unaffected by the scaling are marked green, other cases yellow.

CuFe 300 MPa Unit: 0.001 * mm ³	v = 634 m/s	v = 1600 m/s	v = 2600 m/s
L = 0.4 mm	0.055/0.4 = 0.14	0.048/0.4 = 0.12	0.045/0.4 = 0.11
L = 0.2 mm	0.064/0.2 = 0.32	0.047/0.2 = 0.23	0.045/0.2 = 0.22
Fe 580 MPa Unit: 0.001 * m ³	v = 475 m/s	v = 1600 m/s	v = 2600 m/s
L = 0.8 mm	-	0.66/0.8 = 0.825	-
L = 0.4 mm	0.38/0.4 = 0.95	0.31/0.4 = 0.78	0.050/0.4 = 0.12
L = 0.2 mm	0.19/0.2 = 0.95	0.15/0.2 = 0.75	0.049/0.2 = 0.24

3.5 Material Modeling

The material modeling approach is based on the developments for fragmentation analysis in the previous grant [5]. Isotropic elastic-plastic models are used for both grains and inter-granular boundary material. A simplified variant of the Johnson-Cook model is used, where the yield stress σ_Y is expressed as

$$\sigma_Y = \sigma_{Y0} + B \varepsilon_{pl}^n$$

Here, σ_{Y0} , B and n are constants taken from a material library and ε_{pl} denotes the effective plastic strain. Thus, the material strength is a power law without dependence on strain rate or temperature. In addition, a linear equation of state is assumed. For the tungsten grains, all parameters of the simplified Johnson-Cook model and of the linear equation of state are adapted from the Steinberg-Guinan model and the Mie-Gruneisen equation of state used for the macroscale simulations. For the aluminum grains, the same parameters as in the macroscale simulations were used.

The surrounding border material is modeled with the same material parameters as the grains, except for the yield stress which is reduced by a factor α (Figure 3.4). The factor represents the ratio of inter-granular cohesive strength to grain strength. As this ratio can be influenced by production processes, e. g. by sintering temperature and pressure, different values will be considered in the investigations. The failure of the grain boundaries is modeled via the node-split approach with the effective plastic strain as split criterion. The failure limits of the effective plastic strain are distributed randomly in space with uniform statistical distributions from a chosen interval. This interval needs to be specified as a material parameter.

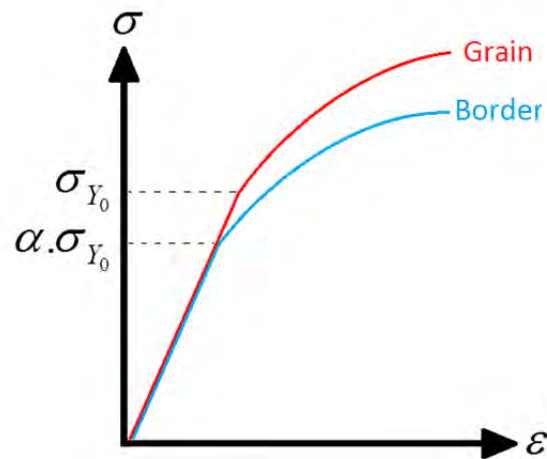


Fig. 3.4: Stress-strain curve of the grains and of border material: identical elastic and hardening process but different yield stresses.

3.6 Initial Selection of Material Data Sets

The launch and impact simulations are carried out with the aim to identify material properties required for a material to both survive explosive launch and fragment upon plate perforation. The following parameters were varied for this purpose:

- Base material (Al, Tun and mixtures of both)
- Grain size distribution
- Porosity
- Grain boundary strength
- Grain boundary failure strain interval

The following tables summarize the parameters for the tungsten and the aluminum sample. At this stage, mixtures of the both materials are not yet considered.

Table 3.4: Material data for tungsten.

Tungsten			
RVE edge length and resolution	L = 0.3 mm n = 40 ³ elements	L = 0.6 mm n = 80 ³ elements	L = 0.9 mm n = 120 ³ elements
Grain distribution	Uniform: D = 30 μ m		Non-uniform: D = [7.5 μ m , 45 μ m]
Porosity	10 %		20 %
Material data of grains and border	ρ = 19.3 g/cm ³ G = 160 GPa K = 313 GPa B = 1.055 GPa n = 0.82		
Yield stress of grains	$\sigma_{Y0}^{\text{grains}} = 2.2$ GPa		
Yield stress of border	Strong border ($\alpha = 80$ %): $\sigma_{Y0} = 1.76$ GPa		Weak border ($\alpha = 30$ %): $\sigma_{Y0} = 0.66$ GPa
Failure strain interval of border	[0.05,0.15]	[0.10,0.30]	[0.20,0.40]

Table 3.5: Material data for aluminum.

Aluminum					
RVE edge length and resolution	L = 0.3 mm n = 40 ³ elements		L = 0.6 mm n = 80 ³ elements		L = 0.9 mm n = 120 ³ elements
Grain distribution	Uniform: D = 30 μm			Non-uniform: D = [7.5 μm , 45 μm]	
Porosity	10 %			20 %	
Material data of grains and border	ρ = 2.76 g/cm ³ G = 25.8 GPa K = 78.5 GPa B = 0.36 GPa n = 0.34				
Yield stress of grains	$\sigma_{Y0}^{\text{grains}}$ = 0.2 GPa		$\sigma_{Y0}^{\text{grains}}$ = 0.4 GPa		$\sigma_{Y0}^{\text{grains}}$ = 0.8 GPa
Yield stress of border	Strong border (α = 80 %): $\sigma_{Y0}^{\text{border}}$ = 0.8 $\sigma_{Y0}^{\text{grains}}$			Weak border (α = 30 %): $\sigma_{Y0}^{\text{border}}$ = 0.3 $\sigma_{Y0}^{\text{grains}}$	
Failure strain interval of border	[0.05,0.15]	[0.1,0.3]	[0.2,0.4]	[0.3,0.6]	[0.4,0.8]

3.7 Launch Modeling

The launch simulations presented in Chapter 2 of this report provide the transient fluid pressures which act on the faces of a cube-shaped pre-formed fragment. To impose these launch conditions on the cube used in the mesoscale simulations, the local pressure transients obtained at the different gauge points were smoothly interpolated on the external faces of the cube as sketched in the following figure:

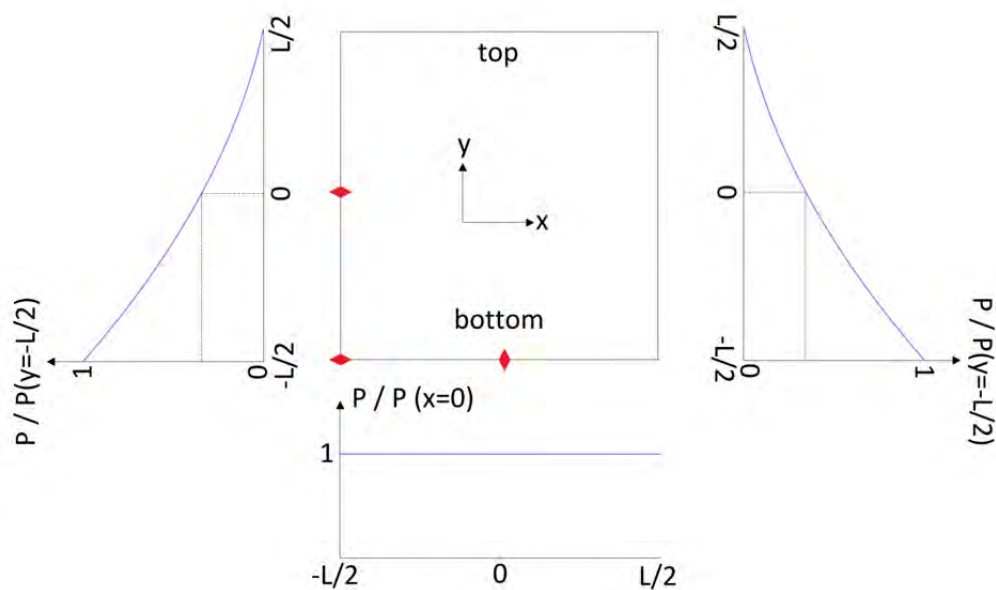


Fig. 3.5: Schematic representation of the pressure profiles acting on the faces of the cube. Pressures are normalized by the pressure values measured at the corresponding gauge points (bottom, left/right below, middle left/right) in the macroscale launch simulations.

The red diamonds indicate positions of the gauge points that measure the surface pressure over time in the macroscale launch simulations. From these measurements, the pressure distribution on the surfaces was interpolated according to two assumptions:

- The bottom face is loaded with a constant distribution on the entire area. The value is given by the corresponding bottom gauge data.
- The four lateral faces have a decreasing pressure profile which start from the "bottom left/right" gauge, covering the "middle left/right" gauge and approach zero at the top face. Thus, the pressure profile follows a quadratic equation, the coefficients of which are determined by the two lateral gauge data and the zero condition at the edge to the top face.

The pressure distribution is applied as time-dependent boundary condition for the cube. Contrary to the macroscale launch simulations, in which all cubes surrounding the explosive charge are modeled, only one cube can be represented in the mesoscale simulations due to the large computational effort. In a first attempt, the lateral confinement by adjacent cubes during the initial acceleration was neglected (compare Figure 2.13). Very large deformations occurred in these simulations at the bottom face edges of the cube.

To reproduce the lateral confinement established through adjacent cubes during the initial stage of the acceleration, symmetry planes were introduced as shown in Figure 3.6. In the 2-D radial plane, the cube is constrained to move within a rigid wedge with its tip in the center of the charge and an opening angle defined by the ratio of 360° and the number of cubes. In axial direction, the cube interaction must also be considered. For this purpose, two parallel rigid surfaces are introduced which constrain the movement and deformation of the simulated cube, see Figure 3.6, right.

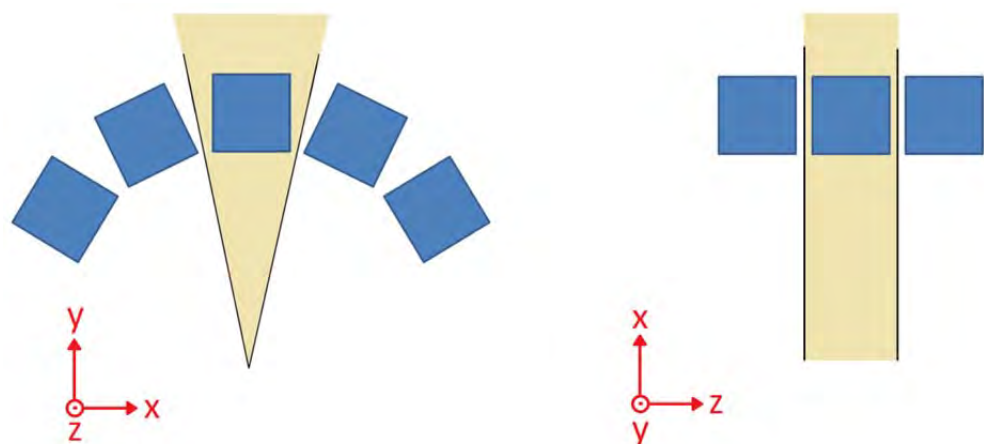


Fig. 3.6: Definition of rigid surfaces around the simulated cube to reproduce the contact to adjacent cubes due to deformation during the launch process. Left: view in the axial direction. Right: view in the radial direction.

Thus, in the single cube model a rigid wedge-shaped funnel surrounds the cube (shown in Figure 3.7) to reproduce the symmetry conditions of the real warhead.

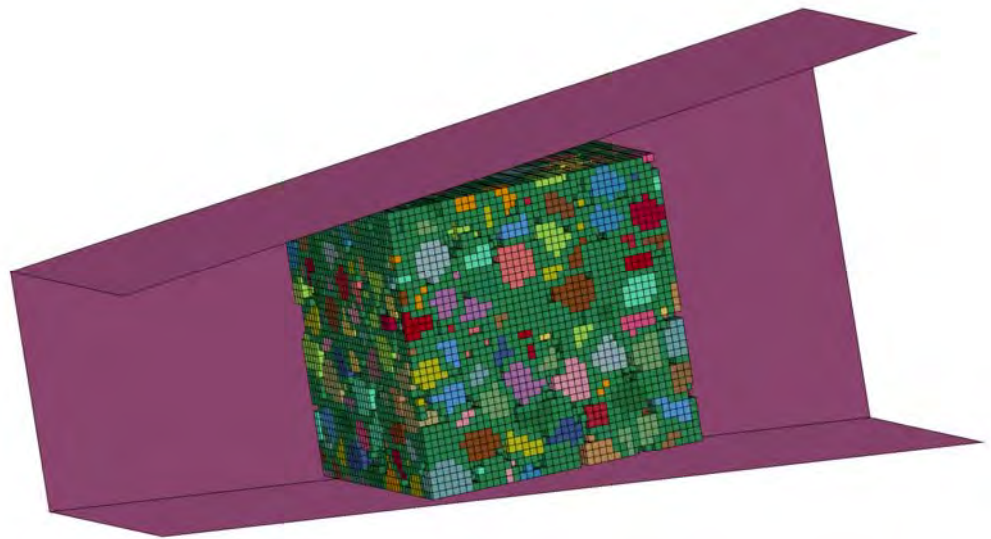


Fig. 3.7: RVE surrounded by a rigid wedge-shaped funnel (cone) to reproduce the symmetry conditions of the real warhead.

3.8 Launch Simulations of a Single Cube

The numerical model for the launch simulations is shown in Figure 3.7. The time-dependent pressure boundary conditions – as described in the previous section – are applied to the six surfaces of the cube using a scaled time (the time scaling being identical to the geometrical scaling). Due to the exerted pressures, the cube is accelerated out of the funnel in x-direction. The final time for the computations was set to $3 \mu\text{s}$ (scaled time). At this time, the RVE has left the funnel by several edge lengths and its state can be evaluated.

The two materials investigated by now are tungsten and aluminum, each with the stronger border material of grain boundary strength, i. e. 1.76 GPa for tungsten and 0.16 GPa for aluminum. The parameter study performed contains the variation of the grain size distribution (uniform or non-uniform), the porosity (10 % porosity or 20 % porosity) and of the failure strain intervals, wherein the failure strain intervals range from 0.05 up to 0.8. Furthermore, for the aluminum RVEs, the yield stress of the aluminum grains is increased by factor 2 and by factor 4, respectively.

The Figure 3.8 shows a typical result for the tungsten RVEs at time $3.0 \mu\text{s}$. At the left side, one can see the end of the funnel. On the right side, the tungsten RVE is recognized to be compressed but almost intact. Only a few fragments can be observed in its surrounding. This figure holds for a RVE of non-uniform grain size distribution with a porosity of 10 %. The failure strain interval ranges from 0.05 to

0.15. All other tungsten RVEs of this study show a very similar damage at final time, the results are summarized in Table 3.6. Generally, it can be stated that the tested tungsten RVEs all survive the launch process with considerable deformation, but only small damage; very few fragments are produced.

For the aluminum RVEs, the obtained results are contrary. The Figures 3.9 and 3.10 show two typical results, in which the aluminum RVEs fragment to a very high degree. The two RVEs shown differ in the failure strain interval and in the yield stress of their grains. For Figure 3.10, the yield stress was set to 0.8 GPa, which is well beyond normal aluminum strength. Even for this stronger material, the RVE can be described as totally damaged; nevertheless the agglomeration of the fragments is more compact as in Figure 3.9, where the aluminum grains are modeled with a (more realistic) yield stress of 0.2 GPa.

The conclusion for the mesoscale launch simulations performed with a single RVE so far is that none of the aluminum RVEs would survive the launch phase. The results are summarized in Table 3.7. The tungsten RVEs, however, all survive the launch, even with low failure strains of the border materials. Grain size distribution and porosities do not significantly affect the results. This is due to the high strength of the tungsten grains and the high boundary strength. At lower boundary strengths (lower α values), the other parameters will influence the results. This will be tested as a next step, along with the two mixtures of aluminum and tungsten.



Figure 3.8: Non-uniform tungsten RVE with porosity 10 %.

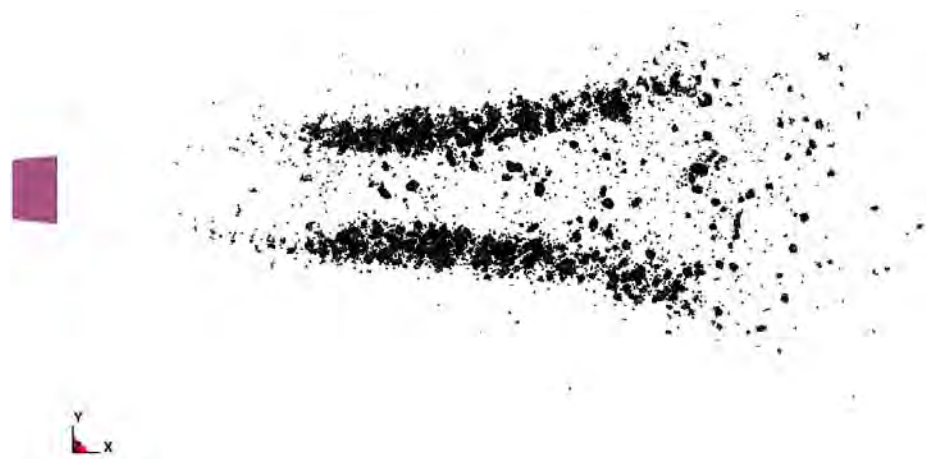


Figure 3.9: Non-uniform aluminum RVE with porosity 10 % and yield stress 0.2 GPa.

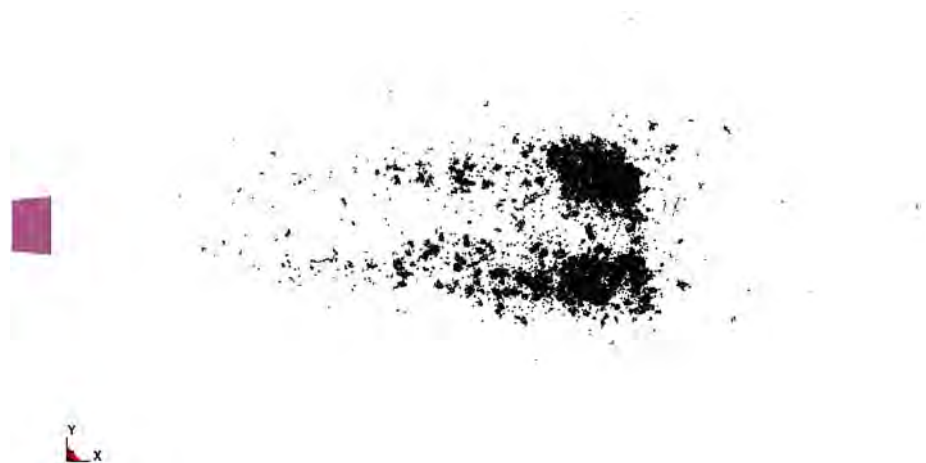


Figure 3.10: Non-uniform aluminum RVE with porosity 10 % and yield stress 0.8 GPa.

Table 3.6: Summary for the launch simulations with tungsten. The final time is $t_{\max} = 3 \mu\text{s}$.

Mat.	Grain size distribution	Porosity [%]	Grain boundary strength [GPa]	Failure strain interval	Results		
					Damage state at t_{\max}	Velocity (t_{\max}) [m/s]	Displacement (t_{\max}) [mm]
Tu	Non-uniform	10	1.76	0.05 to 0.15	Intact, few fragments	1068.69	2.486
Tu	Non-uniform	10	1.76	0.10 to 0.30	Intact, few fragments	1100.56	2.554
Tu	Non-uniform	10	1.76	0.20 to 0.40	Intact, few fragments	1096.71	2.541
Tu	Non-uniform	20	1.76	0.05 to 0.15	Intact, few fragments	1104.12	2.557
Tu	Uniform	10	1.76	0.05 to 0.15	Intact, few fragments	1042.78	2.423
Tu	Uniform	20	1.76	0.05 to 0.15	Intact, few fragments	1075.67	2.487

Table 3.7: Summary for the launch simulations with aluminum. The final time is $t_{\max} = 3 \mu\text{s}$.

Mat.	Grain size distribution	Porosity [%]	Grain boundary strength [GPa]	Failure strain interval	Yield stress of Al [GPa]	Results
						Damage state at t_{\max}
Al	Non-uniform	10	0.16	0.05 to 0.15	0.2	Totally damaged
Al	Non-uniform	10	0.32	0.10 to 0.30	0.4	Totally damaged
Al	Non-uniform	10	0.32	0.20 to 0.40	0.4	Totally damaged
Al	Non-uniform	10	0.32	0.40 to 0.60	0.4	Totally damaged
Al	Non-uniform	10	0.32	0.60 to 0.80	0.4	Totally damaged
Al	Non-uniform	10	0.64	0.20 to 0.40	0.8	Totally damaged
Al	Non-uniform	20	0.16	0.05 to 0.15	0.2	Totally damaged
Al	Uniform	10	0.16	0.05 to 0.15	0.2	Totally damaged
Al	Uniform	20	0.16	0.05 to 0.15	0.2	Totally damaged

3.9 Impact Modeling

The second phase of the process is the impact of the cube onto a target plate. If the cube passes the launch phase without significant damage or fragmentation, it can be further investigated for the plate impact phase. The impact plate consists of aluminum. It is modeled with a Johnson-Cook strength model and a Mie-Gruneisen equation of state, see Table 3.8. The complete Johnson-Cook model describes the yield stress as follows [9]:

$$\sigma_Y = \left(\sigma_{Y0} + B \varepsilon_{pl}^n \right) \left(1 + C \ln \left(\frac{\dot{\varepsilon}}{\dot{\varepsilon}_0} \right) \right) \left(1 - \frac{T - T_{room}}{T_{melt} - T_{room}} \right)$$

Here, C is the strain rate constant, $\dot{\varepsilon}$ and $\dot{\varepsilon}_0$ are the actual and initial strain rates, respectively, and T is the actual temperature.

Table 3.8: Aluminum properties of the impact plate. The data are taken from the AUTODYN material library.

Density	$\rho = 2.76 \text{ g/cm}^3$		
Shear modulus	$G = 25.8 \text{ GPa}$		
Mie-Gruneisen EOS	$C_0 = 5328 \text{ m/s}$	$s_1 = 1.338$	$\Gamma = 2$
Johnson-Cook flow stress	$\sigma_{Y0} = 0.2 \text{ GPa}$	$B = 0.36 \text{ GPa}$	$n = 0.34$
	$C = 0.015$	$\dot{\varepsilon}_0 = 1.e-3 \text{ 1/s}$	$T_{room} = 293 \text{ K}$ $T_{melt} = 775 \text{ K}$
Heat capacity	$C_p = 0.885$		
Failure strain	$\varepsilon_f = 1$		

The numerical model for the impact simulations is shown in Figure 3.11. It is exactly the same approach as for the launch simulations, only the impact plate has been added on the right side. This way, a potential pre-damage from the launch process is automatically accounted for in the impact simulation.

The cube impacts the aluminum plate with the final velocity achieved in the launch phase. This existing velocity between the cube and the aluminum impact plate allows us to let the plate at rest. Other impact velocities and varying angles of attack will be realized by imposing an initial velocity to the plate. This way, any impact scenarios can be analyzed.



Fig. 3.11: Numerical model for impact simulations.



Fig. 3.12: Results of an impact simulation. Rigid funnel, perforated impact plate and partially fragmented tungsten cube at scaled time $6 \mu\text{s}$.

3.10 Launch and Impact Simulations and Fragment Analysis

Figure 3.12 shows a typical result of an impact simulation of a tungsten cube at the scaled time $6 \mu\text{s}$. One can see the hole in the perforated target plate and the partially fragmented RVE on its right. Table 3.9 summarizes the results of the impacts of the tungsten cubes with two different porosities (10 % and 20 %).

Compared to the launch simulations, a variation of the strength of the grain boundary material has been included in the analysis (strength values 1.76 GPa and 0.66 GPa). All following figures are taken and evaluated at a computational time of 6 μ s, while the impact on the plate takes place at 3 μ s. The four cubes show different degrees of fragmentation. The fragmentation increases with increasing porosity and decreasing grain boundary strength. Table 3.10 compiles the data of the four simulations.

Following the procedure for fragment size analysis used in the previous grant, a statistical analysis of the fragmentation is performed by sorting fragments by mass. With a view to conciseness and comprehension, the distribution of fragments is presented in the form of histograms in mass classes. The indicated mass classes give a range of fragment masses, such that class 0.41 μ g contains fragments up to 0.41 μ g, class 0.81 μ g contains fragments from 0.41 μ g to 0.81 μ g, and so on. For each class, the mass of all fragments contained in the class is divided by the whole RVE mass. This mass proportion is represented on the ordinate axis. Currently, only the tungsten RVEs with a non-uniform initial grain distribution were investigated, see Figure 3.13. The mass classes defined were defined according to a logarithmic subdivision.

Table 3.9: Partially fragmented tungsten RVEs at scaled time 6 μ s.

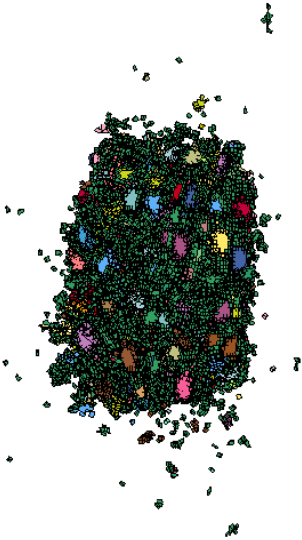
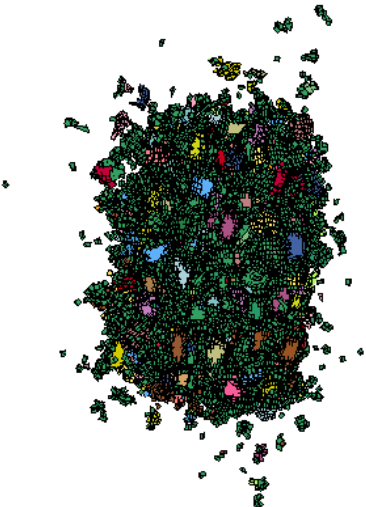
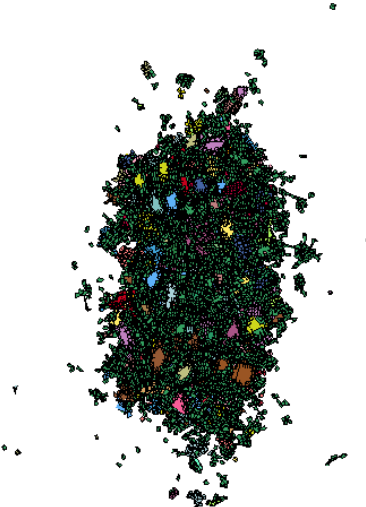
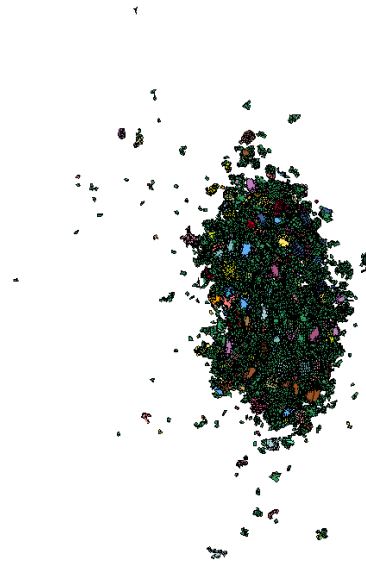
<div>Porosity 10 % Grain bound. strength = 1.76 GPa</div> 	<div>Porosity 20 % Grain bound. strength = 1.76 GPa</div> 
<div>Porosity 10 % Grain bound. strength = 0.66 GPa</div> 	<div>Porosity 20 % Grain bound. strength = 0.66 GPa</div> 

Table 3.10: Summary for the impact simulations with tungsten. The final time is $t_{\max} = 6 \mu\text{s}$.

Mat.	Grain size distribution	Porosity [%]	Grain boundary strength [GPa]	Failure strain interval	Results		
					Damage state at t_{\max}	Velocity (t_{\max}) [m/s]	Displacement (t_{\max}) [mm]
Tu	Non-uniform	10	1.76	0.05 to 0.15	Seriously damaged, many fragments, some larger fragments	1054.73	5.670
Tu	Non-uniform	20	1.76	0.05 to 0.15	Seriously damaged, many fragments, few larger fragments	1052.42	5.807
Tu	Non-uniform	10	0.66	0.05 to 0.15	Seriously damaged, many fragments, few larger fragments	1060.16	5.773
Tu	Non-uniform	20	0.66	0.05 to 0.15	Seriously damaged, many fragments, very few larger fragments	1093.18	5.988

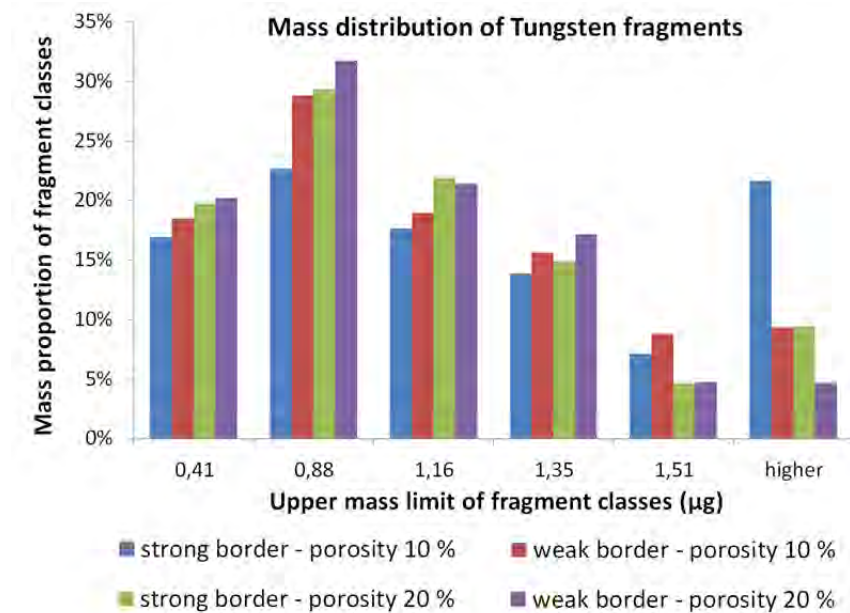


Fig. 3.13: Mass proportion distribution of tungsten fragments with definition in mass classes. Only simulation results for non-uniform initial grain distributions are represented.

From the histogram, two main conclusions can be drawn:

- For the same porosity, the amount of fragments up to 1.63 µg is higher for the weak border than for the strong one. Inversely, the strong border exhibits a higher amount of big fragments (higher masses) than the weak border. This observation agrees with the expected tendency of the strong border not failing as rapidly as the weak border, and accordingly producing less small fragments.
- For a given grain boundary strength, the total amount of fragments up to 1.35 µg increases with increasing porosity, whereas the number of bigger fragments (heavier than 1.63 µg) decreases with increasing porosity. As a lower porosity implies a weaker granular structure, the RVE will be more likely to fragment into small fragments.

These findings are corroborated by an analysis of the average fragment size, which we define here as the median of the fragment mass distribution. A fragmentation ratio can be quantitatively defined as follows:

$$FR = \frac{\text{number of 'cracks'}}{\text{maximum number of possible 'cracks'}} = \frac{\text{number of fragments} - 1}{\text{number of grains} - 1}$$

Here “cracks” are defined as complete separation of two groups of (or individual), grains. The number of these cracks is directly related to the number of fragments they produce. The maximum number of possible cracks corresponds to a full fragmentation, for which all fragments are exactly the original grains. For instance, a structure composed of three grains can fragment in the following manner:

- A “crack” separates a group of two grains from an individual grain, in which case one has two fragments (for three initial grains) and

$$FR = \frac{2-1}{3-1} = 0.5 \text{ (or 50\%) .}$$
- A second crack separates the group of two grains, the fragmentation is then complete and $FR = \frac{3-1}{3-1} = 1 \text{ (or 100\%) .}$

The median fragment mass and the fragmentation ratio are represented for each structure in Table 3.11.

Table 3.11: Tungsten with non-uniform initial grain distribution: median fragment mass and fragmentation percentage.

	Median fragment mass [μg]	Fragmentation percentage
Strong border Porosity 10 %	1.05	88.17 %
Weak border Porosity 10 %	0.94	94.27 %
Strong border Porosity 20 %	0.90	91.76 %
Weak border Porosity 20 %	0.86	92.43 %

The results for median fragment mass in the table confirm the interpretation of the fragment mass histogram, i. e., the median fragment mass tends to decrease with increasing porosity on the one hand, with increasing border weakness on the other hand.

Concerning the fragmentation percentage, at a fixed porosity a higher fragmentation percentage is obtained for a weaker border, which confirms the previous results. No clear tendency is observed for the fragmentation ratio is observed for porosity variation at fixed border strength. However, considering the fact that all observed fragmentation results are pretty close to complete fragmentation (100 %) the fluctuation might be due to the completely different RVEs which were generated to vary the porosity.

4 Conclusions and Next Steps

The principal goal of the ongoing research is to identify by numerical mesoscale simulations which properties (grain sizes, porosities, strength etc.) a cube with 1 cm edge length made of a sintered mixture of aluminum and tungsten would need to survive an explosive launch in a warhead and fragment into as many small particles as possible upon perforation of a thin aluminum plate. Such a material would be a promising candidate for a future use as reactive material in anti-aircraft or anti-missile warhead shells. In the period documented in this intermediate report, several methodological questions have been solved and first material variants were investigated in numerical simulations. Macroscale simulations were used to generate transient pressure data as boundary condition for the mesoscale analyses of an explosive launch of a RVE. A downscaling approach for mesoscale analysis has been developed, first results indicate its applicability, further verification is still in progress. The scaling seems to be valid as long as the generated fragments are small compared to the sample size, where small means that characteristic lengths differ by about a factor of at least 4. A methodology for the mesoscale modeling of launch and subsequent impact on a target plate has been established. An initial series of simulations has been performed and evaluated. In accordance with general experience in warhead design, it turned out that pure aluminum compositions are not suitable as candidates as they fragment already during the explosive launch, even if very high grain and inter-granular strength values are assumed. Tungsten, instead, is suitable as base material, in the simulations performed so far, samples with high (1.76 GPa) and lower (0.66 GPa) grain boundary strength and porosities of 10 % and 20 % survived launch and yielded a high degree of fragmentation. As would be expected, the highest degree of fragmentation was obtained for the higher porosity and lower grain boundary strength.

The most important next steps will be launch and impact simulations for a variety of material compositions, including mixtures of aluminum and tungsten, and variation of material parameters, especially grain boundary strength (**task 2**, Figure 1.2). In the course of this work, the dependency on mesoscale parameters of both the resistance of materials in launch and impact simulations and the fragment size distribution after impact will be investigated systematically. The goal is to identify material mixtures with optimal properties which could be realized by sintering aluminum and tungsten powders. Next, we want to provide recommendations on preferable mesoscale parameters based on fragment size distributions, and we want to derive homogenized stress-strain relationships for the recommended material(s). The latter shall be done in order to provide a reference for comparisons with other materials. As a result of the investigations on scaling (**task 1**, Figure 1.2),

the chosen scaling must be checked carefully at each future fragmentation computation, and the RVE size must be adapted if necessary.

Finally, launch and impact simulations for selected materials with different impact velocities, plate materials, plate thicknesses and with various angles of attack to the impact plate will be performed as well as the analysis of the dependency of fragmentation on the impact parameters (**task 3**, Figure 1.2). This way, the best performing materials are checked for their behavior under different impact conditions in order to gain information on the robustness of the material design.

5 Literature

- [1] Heilig, G.; Durr, N.; Sauer, M.; Klomfass, A.: *"Mesoscale Analysis of Sintered Metals Fragmentation under Explosive and Subsequent Impact Loading"*, Abstract submitted to HVIS2012, Baltimore, Maryland, September 16–20, 2012
- [2] Klomfass, A.; Bagusat, F.; Durr, N.; Heilig, G.; Knell, S.; Sauer, M.: *"Mesoscale Mechanics of Reactive Materials for Enhanced Target Effects"*, Report prepared for the 2011 Peer review of the Office of Naval Research 351 Advanced Energetics Materials and Advanced Combustion Program, National Harbor, MD, September 13–14, 2011
- [3] Neuwald, P.; Reichenbach, H.; Kuhl, A.: *"Combustion of Shock-Dispersed Aluminum – Some Parametric Studies"*, 19th MABS, Calgary, 2006
- [4] Nossek, M.; Sauer, M.; Thoma, K.: *"Adaptive Simulation of Cohesive Interface Debonding for Crash- and Impact Analyses"*, Proceedings of the 3rd European Conference on Computational Mechanics: Solids, Structures and Coupled Problems in Engineering, Lissabon, 2006
- [5] Raftenberg, M. N.; Mock, W. Jr.; Kirby, G. C.: *"Modeling the Impact Deformation of Rods of a Pressed PTFE/Al Composite Mixture"*, Int. J. Imp. Eng. 35(12), 2008, pp. 1537–1544
- [6] Sauer, M.; Klomfass, A.; Bagusat, F.; Durr, N.; Knell, S.; Linnemann, K.: *"Characterization of the Material Microstructure for Reactive Material Design"*, (ONR grant N00014-07-1-1053 final report). Fraunhofer Institute for High-Speed Dynamics, Ernst-Mach-Institut, EMI, Freiburg, Germany, Report I-14/10, 2010
- [7] Sauer, M.; Bagusat, F.; Durr, N.; Klomfass, A.: *"Fragmentation of Partially Sintered Materials – Experimental Investigation and Mesoscale Simulation"*, Proceedings of the Hyper Velocity Impact Symposium HVIS 2010, Freiburg, Germany
- [8] Steinberg, D. J.: *"Equation of State and Strength Properties of Selected Materials"*, Lawrence Livermore National Laboratory, February 13, 1991
- [9] Johnson, G. R.; Cook, W. H.: *"A Constitutive Model and Data for Metals Subjected to Large Strains, High Strain Rates and High Temperatures"*, Proc. 7th Int. Symposium on Ballistics, The Hague, Netherlands, 1983

List of Distribution

Report No. I-56/11

Author: Georg Heilig, Nathanael Durr

Title: Mesoscale Mechanics of Reactive Materials for Enhanced Target Effects
– Performance/Technical Report 2011

Internal Distribution:

Author(s): G. Heilig, N. Durr, M. Sauer, A. Klomfass

External Distribution:

Clifford Bedford, Ph.D. 1 Hardcopy + CD
Program Manager Code 351
Advanced Energetics Materials
Office of Naval Research
875 N. Randolph St.
Arlington, VA 22203-1995

Dr. Judah Goldwasser PDF
DARPA/DSO
3701 North Fairfax Dr
Arlington, VA 22203
Judah.Goldwasser@darpa.mil

Defense Technical Information Center 1 Hardcopy + CD
8725 John J Kingman Road Ste 0944
Fort Belvoir, VA 22060-6218

ONR REG BOSTON N62879 1 Hardcopy + CD
495 Summer Street Room 627
Boston, MA 02210-2109

Naval Research Laboratory
ATTN: CODE 5596
4555 Overlook Avenue SW
Washington, DC 20375-5320

1 Hardcopy + CD

REPORT DOCUMENTATION PAGE			Form Approved OMB No. 0704-0188		
Public reporting burden for this collection of information is estimated to average 1 hour per response, including the time for reviewing instructions, searching existing data sources, gathering and maintaining the data needed, and completing and reviewing this collection of information. Send comments regarding this burden estimate or any other aspect of this collection of information, including suggestions for reducing this burden to Department of Defense, Washington Headquarters Services, Directorate for Information Operations and Reports (0704-0188), 1215 Jefferson Davis Highway, Suite 1204, Arlington, VA 22202-4302. Respondents should be aware that notwithstanding any other provision of law, no person shall be subject to any penalty for failing to comply with a collection of information if it does not display a currently valid OMB control number. PLEASE DO NOT RETURN YOUR FORM TO THE ABOVE ADDRESS.					
1. REPORT DATE (DD-MM-YYYY) 31-12-2011		2. REPORT TYPE Performance/Technical Report		3. DATES COVERED (From - To) July - December 2011	
4. TITLE AND SUBTITLE Mesoscale Mechanics of Reactive Materials for Enhanced Target Effects			5a. CONTRACT NUMBER		
			5b. GRANT NUMBER N00014-11-1-0307		
			5c. PROGRAM ELEMENT NUMBER		
6. AUTHOR(S) Georg Heilig, Nathanael Durr, Martin Sauer, Arno Klomfass			5d. PROJECT NUMBER 11PR04524-01		
			5e. TASK NUMBER		
			5f. WORK UNIT NUMBER		
7. PERFORMING ORGANIZATION NAME(S) AND ADDRESS(ES) Fraunhofer Institute for High-Speed Dynamics Ernst-Mach-Institut, EMI Eckerstrasse 4 79104 Freiburg Germany			8. PERFORMING ORGANIZATION REPORT NUMBER I-56/11		
9. SPONSORING / MONITORING AGENCY NAME(S) AND ADDRESS(ES) Carol A. Porter / Clifford D. Bedford Office of Naval Research 875 North Randolph Street Arlington, VA 22203-1995			10. SPONSOR/MONITOR'S ACRONYM(S) ONR BD025 / ONR 351		
			11. SPONSOR/MONITOR'S REPORT NUMBER(S)		
12. DISTRIBUTION / AVAILABILITY STATEMENT approved for public release					
13. SUPPLEMENTARY NOTES					
14. ABSTRACT The research documented in this report concerns the mechanical behavior of sintered reactive metal compositions for potential use in shells of explosive warheads. The technical goal of the research is to determine by numerical simulations which mechanical properties cubes of sintered mixtures of aluminum and tungsten would need to survive an explosive launch and fragment into small combustible particles after penetration of a thin aluminum sheet. A methodology has been developed to determine the loads during explosive launch from macroscale, fluid-structure coupled simulations. These loads are applied as boundary conditions for mesoscale simulations of launch, impact and fragmentation using mesoscale models of the material, representative volume elements. A first set of materials is regarded, pure aluminum and pure tungsten compositions with varying intergranular strengths, porosities and grain size distributions. Whereas all aluminum based materials considered so far are too weak to survive the explosive launch, tungsten based materials perform better. For the latter materials, distributions of fragment size after impact are determined from simulations. As next step, launch and impact simulations for mixtures of Aluminum and Tungsten with varying parameters will be performed in order to quantify the properties required for suitable reactive material compositions.					
15. SUBJECT TERMS reactive materials, sintered metals, fragmentation, mesoscale, numerical simulation					
16. SECURITY CLASSIFICATION OF:			17. LIMITATION OF ABSTRACT	18. NUMBER OF PAGES 54	19a. NAME OF RESPONSIBLE PERSON Arno Klomfass
a. REPORT	b. ABSTRACT	c. THIS PAGE			19b. TELEPHONE NUMBER (include area code) ++49-761-2714-313